

**COMPARATIVE STUDY OF CARDIAC IMAGING QUALITY  
WITH AND WITHOUT TRANSMISSION CORRECTION**



**A THESIS SUBMITTED IN PARTIAL FULFILLMENT  
OF THE REQUIREMENTS FOR  
THE DEGREE OF MASTER OF SCIENCE  
(RADIOLOGICAL SCIENCE)  
FACULTY OF GRADUATE STUDIES  
MAHIDOL UNIVERSITY  
2008**

**COPYRIGHT OF MAHIDOL UNIVERSITY**

Copyright by Mahidol University

Thesis  
Entitled

**COMPARATIVE STUDY OF CARDIAC IMAGING QUALITY  
WITH AND WITHOUT TRANSMISSION CORRECTION**



*Ruentip Tipparoj*  
.....  
Miss Ruentip Tipparoj  
Candidate

*Rujaporn Chanachai*  
.....  
Assoc.Prof. Rujaporn Chanachai, Ph.D.  
Major-Advisor

*Vacharin Ratanamart*  
.....  
Assoc.Prof. Vacharin Ratanamart, M.D.  
Co-Advisor

*Pachee Chaudakshetrin*  
.....  
Miss Pachee Chaudakshetrin, M.Eng.  
Co-Advisor

*Thongpraparn*  
.....  
Mr. Thonnapong Thongpraparn, M.Eng.  
Co-Advisor


*B. Mahaisavariya*  
.....  
Prof. Banchong Mahaisavariya,  
M.D.  
Dean  
Faculty of Graduate Studies.

*N. Sritongkul*  
.....  
Assoc.Prof. Nopamon Sritongkul,  
M.Sc. (Biochem.)  
Chair  
Master of Science Programme in  
Radiological Science  
Faculty of Medicine Siriraj Hospital.

Thesis  
Entitled

**COMPARATIVE STUDY OF CARDIAC IMAGING QUALITY  
WITH AND WITHOUT TRANSMISSION CORRECTION**

was submitted to the Faculty of Graduate Studies, Mahidol University for the degree  
of Master of Science (Radiological Science)  
on  
3 October 2008



Miss Ruentip Tipparoj  
Candidate



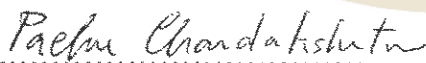
Assoc. Prof. Laorthip Chanachai,  
Ph.D.  
Chair



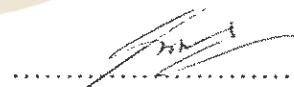
Assoc. Prof. Rujaporn Chanachai,  
Ph.D.  
Member



Assoc. Prof. Vacharin Ratanamart,  
M.D.  
Member



Miss Pachee Chaudakshetrin,  
M. Eng.  
Member



Mr. Thonnapong Thongpraparn,  
M. Eng.  
Member



Prof. Banchong Mahaisavariya,  
M.D.  
Dean  
Faculty of Graduate Studies  
Mahidol University.



Clin. Prof. Teerawat Kultanan, M.D.,  
F.I.M.S., F.R.C.S.T., F.I.C.S.  
Dean  
Faculty of Medicine Siriraj Hospital  
Mahidol University.

## ACKNOWLEDGEMENTS

The success of this thesis can be attributed to the extensive support and assistance from my major advisor, Assoc. Prof. Dr. Rujaporn Chanachai and my co-advisor, Assoc. Prof. Vacharin Ratanamart, Ms. Pachee Chaudakshetrin, and Mr.Thonnapong Thongpraparn. I would like to express my gratitude for the improvements that they made possible. I also thank to my thesis committee, Assoc. Prof. Dr. Laorthip Chanachai, for her editorial assistance.

My special thank to Dr. Glenn SY, GE Healthcare, for explaining about the algorithm of Myovation.

I would like to thank the staff of Division of Nuclear Medicine, Siriraj Hospital for their invaluable advice and kind support.

Finally, I thank my family for educating me, their unconditional support, entirely care and love.

Ruentip Tipparoj

**COMPARATIVE STUDY OF CARDIAC IMAGING QUALITY WITH AND WITHOUT TRANSMISSION CORRECTION**

RUENTIP TIPPAROJ 4636160 SIRS/M

M.Sc. (RADIOLOGICAL SCIENCE)

THESIS ADVISORS: RUJAPORN CHANACHAI, Ph.D. (BIOPHYSICS),  
VACHARIN RATANAMART, M.D., PACHEE CHAUDAKSHETRIN, M.Eng.  
(NUCLEAR TECHNOLOGY), THONNAPONG THONGPRAPARN, M.Eng.  
(NUCLEAR TECHNOLOGY)

**ABSTRACT**

Coronary artery disease (CAD) is the most common heart disease and leads to myocardial ischemia and myocardial infarctions. Myocardial perfusion SPECT imaging is used for diagnosis of CAD. However, there are several important factors which reduce the quality of the images and can lead to misinterpretation. Differences in patients' shape and size can result in different photon attenuation as well as scatter. The purpose of this study was to study the effects of attenuation correction on image quality of myocardial perfusion SPECT by comparison between an iterative reconstruction technique (IRAC) and non-attenuation correction (IRNC). The percentage of threshold level, number of subsets, and activity distribution parameters were optimized. The method in this study was divided into two steps myocardial perfusion SPECT acquisition in 1) anthropomorphic torso phantom and 2) 20 normal patients (male = 10 and female = 10). The optimal parameter of percentage threshold level and number of subsets were applied to create 40 myocardial perfusion SPECT images. Following this, the sensitivity, specificity, and accuracy of all images were analyzed. The results revealed that at 50% threshold level and 10 subsets an accurate size of defect was obtained. There were statistically significant differences in the uniformity of count distribution between IRAC and IRNC techniques (p-value < 0.001). The sensitivity, specificity, and accuracy of IRAC image were 72.5%, 85%, and 78.75% respectively. The sensitivity, specificity and accuracy of IRNC image were 67.5%, 60%, and 64.25%, respectively. In conclusion, myocardial perfusion SPECT imaging with attenuation correction technique (IRAC) can improve image quality to a greater degree non-attenuation correction (IRNC), (p-value < 0.001) and increase the interpretation efficiency of myocardial perfusion SPECT imaging for diagnosing myocardial ischemia and myocardial infarctions. Using this method would therefore improve the diagnosis of CAD.

**KEY WORDS:** ATTENUATION CORRECTION / MYOCARDIAL PERFUSION  
SPECT / ITERATIVE RECONSTRUCTION

75 pp.

การศึกษาเพื่อเปรียบเทียบคุณภาพของภาพตัดขวางกล้ามเนื้อหัวใจโดยใช้และไม่ใช้การชดเชยค่า  
แก้

(COMPARATIVE STUDY OF CARDIAC IMAGING QUALITY WITH AND  
WITHOUT TRANSMISSION CORRECTION)

เรื่อนทิพย์ ทิพโรจน์ 4636160 SIRS/M

วท.ม.(วิทยาศาสตร์รังสี)

คณะกรรมการควบคุมวิทยานิพนธ์ : รุจพร ชนะชัย, Ph.D. (Biophysics), วัชรินทร์ รัตนมาศ,  
M.D., พจี เจาทะเกษตริน, M.Eng.(Nuclear Technology), ธนพงษ์ ทองประพาพ, M.Eng.  
(Nuclear Technology)

บทคัดย่อ

โรคเกี่ยวกับหลอดเลือดเลี้ยงหัวใจ (Coronary artery disease) เป็นโรคที่พบบ่อย ส่วนใหญ่เกิดจาก  
กล้ามเนื้อหัวใจขาดเลือด (Ischemic heart) และนำไปสู่ภาวะกล้ามเนื้อหัวใจตาย (Myocardial infraction)  
ซึ่งเป็นสาเหตุทำให้ผู้ป่วยตาย ปัจจุบันได้มีการตรวจกล้ามเนื้อหัวใจตายด้วยวิธี Myocardial Perfusion ด้วย  
เครื่อง SPECT แต่เนื่องจากผู้ป่วยที่มารับการตรวจนั้นมีลักษณะทางกายวิภาคศาสตร์ที่ไม่เหมือนกัน ทำให้มีการ  
ดูดกลืนรังสี (Photon Attenuation) และ การกระเจิง (Scatter) ที่แตกต่างกันด้วย วัตถุประสงค์ของการศึกษานี้  
คือเพื่อเปรียบเทียบคุณภาพของภาพตัดขวางกล้ามเนื้อหัวใจโดยใช้การชดเชยค่าแก้ (Iterative reconstruction  
attenuation correction, IRAC) และไม่ใช้การชดเชยค่าแก้ (Iterative reconstruction non attenuation  
correction, IRNC) โดยหาค่า % threshold level และ จำนวน subset ที่เหมาะสมซึ่งเป็นตัวชี้วัดการกระจาย  
ค่านับวัดรังสีเพื่อใช้ในการสร้างภาพตัดขวางของกล้ามเนื้อหัวใจ วิธีการศึกษาคือหาค่า %Threshold level และ  
จำนวน subset ที่เหมาะสมจากการสร้างภาพตัดขวางของกล้ามเนื้อหัวใจโดยใช้หุ่นจำลองที่มีรอยโรคและไม่มี  
รอยโรค แล้วนำมาสร้างภาพของคนปกติ จำนวน 20 คน แบ่งเป็นชาย 10 คน และหญิง 10 คน หลังจากนั้นนำผล  
การวินิจฉัยของผู้ป่วยจำนวน 40 รายหาค่าความไว ความจำเพาะ ความถูกต้องของทั้ง 2 วิธี ผลการศึกษาพบว่า %  
threshold level ที่ 50 % และ จำนวน subset เท่ากับ 10 นั้นสามารถหาขนาดของรอยโรคของหุ่นจำลองได้ดี  
ที่สุด เมื่อนำมาศึกษาในคนปกติ พบว่าโดยวิธี IRAC นั้นมีความสม่ำเสมอของการกระจายค่านับวัดดีกว่าวิธี  
IRNC อย่างมีนัยสำคัญทางสถิติ (p-value < 0.001) และผลการวินิจฉัยของวิธี IRAC มีค่าความไว  
ความจำเพาะ และความถูกต้องเท่ากับ 72.5% 85% และ 78.75% ตามลำดับ ส่วนผลการวินิจฉัยของวิธี IRNC  
มีค่าความไว ความจำเพาะ และความถูกต้องเท่ากับ 67.5% 60% และ 64.25% ตามลำดับ ดังนั้นสรุปได้ว่า  
ภาพตัดขวางกล้ามเนื้อหัวใจโดยใช้การชดเชยค่าแก้มีคุณภาพมากกว่าการไม่ใช้การชดเชยค่าแก้อย่างมีนัยสำคัญ  
ทางสถิติ (p-value < 0.001) และสามารถใช้นำไปสร้างภาพตัดขวางของกล้ามเนื้อหัวใจเพื่อวินิจฉัยโรคกล้ามเนื้อ  
หัวใจขาดเลือดและกล้ามเนื้อหัวใจตายได้

## CONTENTS

	<b>Page</b>
ACKNOWLEDGEMENTS	iii
ABSTRACT	iv
LIST OF TABLES	vii
LIST OF FIGURES	viii
LIST OF ABBREVIATIONS	xii
CHAPTER	
I    INTRODUCTION	1
II   OBJECTIVE	7
III  LITERATURE REVIEWS	8
IV  MATERIALS AND METHODS	28
V   RESULTS	38
VI  DISCUSSION	56
VII CONCLUSION	58
REFERENCES	59
APPENDIX	63
BIOGRAPHY	75

## LIST OF TABLES

<b>TABLES</b>	<b>Page</b>
1. Tc-99m activity distribution in the organ.	33
2. Area and size of defect between IRNC and IRAC myocardial SPECT images for each threshold level.	39
3. Area and size of defect between IRNC and IRAC myocardial SPECT images for each iteration.	42
4. Area and size of defect between IRNC and IRAC myocardial SPECT images for each number of subset.	43
5. Percentage contrast between IRNC and IRAC myocardial SPECT images of defect phantom studies.	43
6. Percentage normalization from polar map with IRNC and IRAC in phantom studies.	46
7. Percentage of normalization form polar map with IRNC and IRAC in 10 male patients.	48
8. Percentage of normalization from polar map with IRNC and IRAC in 10 female patients.	51
9. Data resulting from observer 1.	53
10. Data resulting from observer2.	54
11. Sensitivity, specificity and accuracy for two observers interpreting the myocardial perfusion image using IRNC and IRAC techniques.	55

## LIST OF FIGURES

FIGURES	Page
1. Physical factors that compromise SPECT are as follow: A. non-uniform attenuation, B. Compton scatter, and C. varying resolution.	2
2. A low resolution CT scan generated for attenuation correction in a SPECT/CT system.	12
3. Tomographic reconstruction of point source (A), by linear superimposition of back-projection (LSBP) (B), and linear superimposition of filter back-projection (LSBP) (C and D), V= frequency.	13
4. Ramp filter in frequency domain (left) and corresponding spatial domain filter (right). Ramp filter is Fourier transform of spatial domain filter, which in turn is inverse Fourier transform of ramp filter.	14
5. Flowchart of iterative method.	16
6. Graphical representation of the iterative reconstruction process. (from Distance Assisted Training Programme for Nuclear Medicine Technologists).	16
7. An alterative way to draw a sine wave (from Distance Assisted Training Programme for Nuclear Medicine Technologists).	17
8. The Fourier transform: the function represented in (A) consisting of the sum three sine waves of different frequencies and amplitude also (B). They can be plotted on an alternative set of axes: amplitude versus frequency (C). Such the plot is the Fourier transform of the original curve, which simply illustrated those frequencies that weighted by the respective amplitudes, sum to provide the original curve.	18

## LIST OF FIGURES (continued)

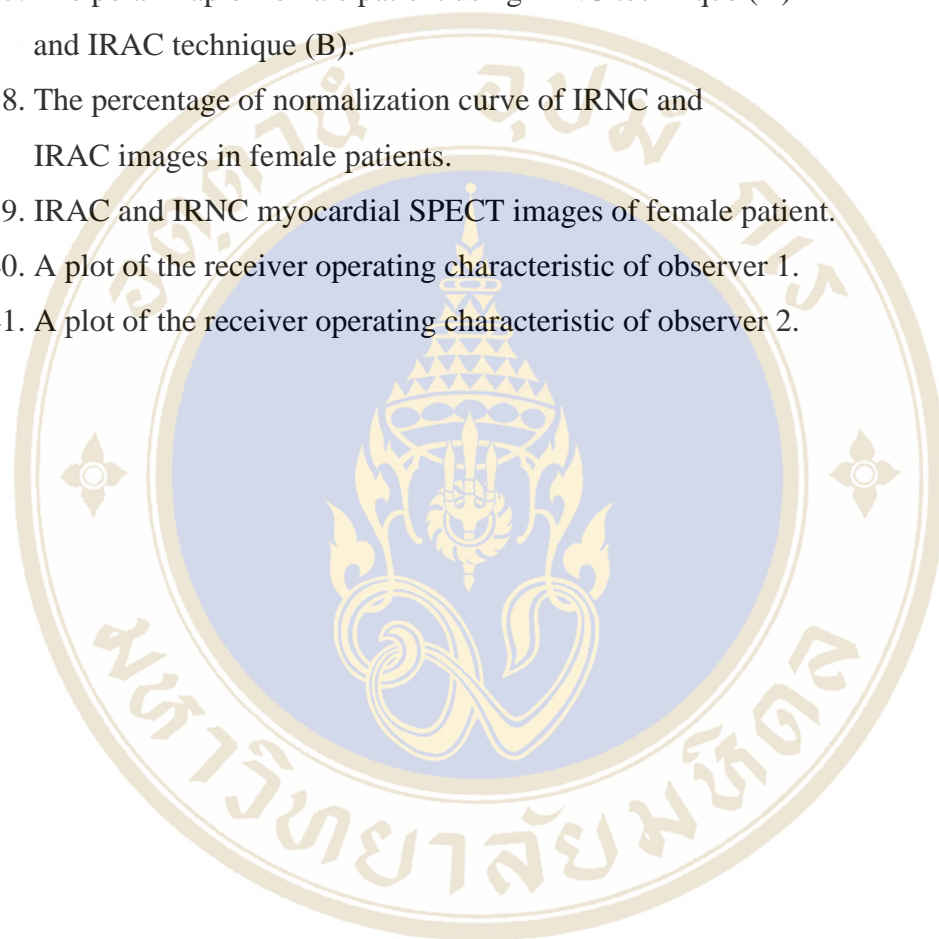
FIGURES	Page
9. Unit for representing frequency (from Distance Assisted Training Programme for Nuclear Medicine Technologists).	20
10. A plot of a ramp filter in frequency space.	21
11. Butterworth filter with parameters $n = 0.5$ and $f_c = 0.33$ .	23
12. If one considered the chest a cube, then the heart is located in its own cube within the large chest cube. The heart (and the heart cube) is pointing downwards, to the left, and anterior. Usually about 45 degree in each direction, but there are considerable individual variations.	24
13. Illustration of the reconstructed cuts perpendicular to the long axis (coronal = short axis cuts) and perpendicular to the short axis (sagittal = axis and horizontal = transaxial cuts).	24
14. Illustration of Short axis slices, from base to apex.	25
15. Illustration of Vertical long axis, LV septum to free wall.	25
16. Illustration of Horizontal long axis, LV anterior to inferior.	26
17. SPECT/CT System, Model H3000 YM Infinia Hawkeye.	28
18. The Anthropomorphic phantom Model ECT/TOR/P, (Data Spectrum Corporation) in various view, (a) frontal view, (b) lateral view, (c) top view, and (d) bottom view.	29
19. The cardiac insert Model ECT/TOR/I, (Data Spectrum Corporation).	30
20. Myocardial solid defect sets.	31
A. The defects with 1.0 cm wall thickness, $60^\circ \times 2$ cm length.	
B. The defects with 1.0 cm wall thickness, $45^\circ \times 1.5$ cm length.	
21. The dose calibrator, Capintec (model CRC15R).	31
22. Diagram of count distribution showing segment observed in the short-axis, vertical long-axis view of myocardium.	36

## LIST OF FIGURES (continued)

<b>FIGURES</b>	<b>Page</b>
23. The reconstructed myocardial SPECT images of cardiac phantom by using IRNC technique for each threshold level.	38
24. The reconstructed myocardial SPECT images of cardiac phantom by using IRAC technique for each threshold level.	39
25. The reconstructed myocardial SPECT images of cardiac phantom by using IRNC technique for each iteration with 10 subset.	40
26. The reconstructed myocardial SPECT images of cardiac phantom by using IRAC technique for each iteration with 10 subset.	41
27. The reconstructed myocardial SPECT images of cardiac phantom by using IRNC technique for each number of subset with 2 iterations.	41
28. The reconstructed myocardial SPECT images of cardiac phantom by using IRAC technique for each number of subset with 2 iterations.	42
29. The percentage contrast curve of IRNC and IRAC images in phantom studies.	44
30. IRAC and IRNC myocardial SPECT images of phantom with solid defect in lateral region of myocardial.	44
31. The polar map of phantom using IRNC technique (A) and IRAC technique (B).	45
32. The percentage of normalization curve of IRNC and IRAC images in phantom studies.	46
33. IRAC and IRNC myocardial SPECT images of defect-free phantom in lateral region of myocardial.	47
34. The polar map of male patient using IRNC technique (A) and IRAC technique (B).	48
35. The percentage of normalization curve of IRNC and IRAC images in male patients.	49
36. IRAC and IRNC myocardial SPECT images of male patient.	49

**LIST OF FIGURES (continued)**

<b>FIGURES</b>	<b>Page</b>
37. The polar map of female patient using IRNC technique (A) and IRAC technique (B).	50
38. The percentage of normalization curve of IRNC and IRAC images in female patients.	51
39. IRAC and IRNC myocardial SPECT images of female patient.	52
40. A plot of the receiver operating characteristic of observer 1.	53
41. A plot of the receiver operating characteristic of observer 2.	54



## LIST OF ABBREVIATIONS

Abbreviation	Term
AC	Attenuation Correction
CAD	Coronary Artery Disease
CT	Computed Tomography
ECG	Electrocardiogram
FBP	Filtered Back Projection
FWHM	Full Width at Half Maximum
FT	Fourier Transform
IRAC	Iterative Reconstruction Attenuation Correction
IRNC	Iterative Reconstruction Non Attenuation Correction
LPO	Left Posterior Oblique
OSEM	Ordered Subset Expectation Maximization
MLEM	Maximum Likelihood Expectation Maximization
NC	Non Attenuation Correction
RAO	Right Anterior Oblique
ROC	Receiver Operating Characteristic Curve
SPECT	Single Photon Emission Computed Tomography
Tl-201	Thallium 201
Tc-99m MIBI	Technetium-99m Methoxyisobutyl-Isonitrite

## CHAPTER I

### INTRODUCTION

#### 1. 1 Background

Myocardial stress perfusion imaging is widely used as non-invasive detection the presence and extent of coronary artery disease (CAD). Although perfusion imaging with SPECT has been shown to be highly sensitive in the detection of CAD, its specificity in assessing the absence of disease has been suboptimal. It has been hypothesized that the suboptimal specificity of myocardial SPECT perfusion imaging is due to the inhomogeneous attenuation of photons in the thorax, which produces artifactual heterogeneous radionuclide distributions in the myocardium of patients without evidence of CAD. Although guidelines have been adopted to distinguish attenuation artifacts from real perfusion abnormalities, photon attenuation reduces the discriminating capacity of myocardial SPECT, resulting in lower test specificity.

A problem in conventional radionuclide imaging is that the obtaining images are two dimensional projections of three dimensional source distributions. Images of the organ structures at one depth in the patient thus are performed by images of overlying and underlying structures. Determining the shape of the distribution requires that the physician assimilates the information into several views. Computed tomography helps to overcome such the problem by using several planar images to reconstruct tomographic images in which each pixel represents a single point within the subject. The pixels actually represent a small volume, often called a voxel. In order to overcome the limitation of the planar images, the first single-head SPECT system was developed in the mid 1970s using circular orbits in which the camera rotated, supported by a ring or gantry, about a motionless patient lying on the bed.

## 1.2 Physical Factor Influencing SPECT Quality

Physical interactions of photon in the patients by Compton scattering, photoelectric absorption, and the effect of collimated detector on the spatial resolution are significant factors affecting the quality of SPECT images. Such the factors influencing SPECT images are so complex that will be discussed separately.

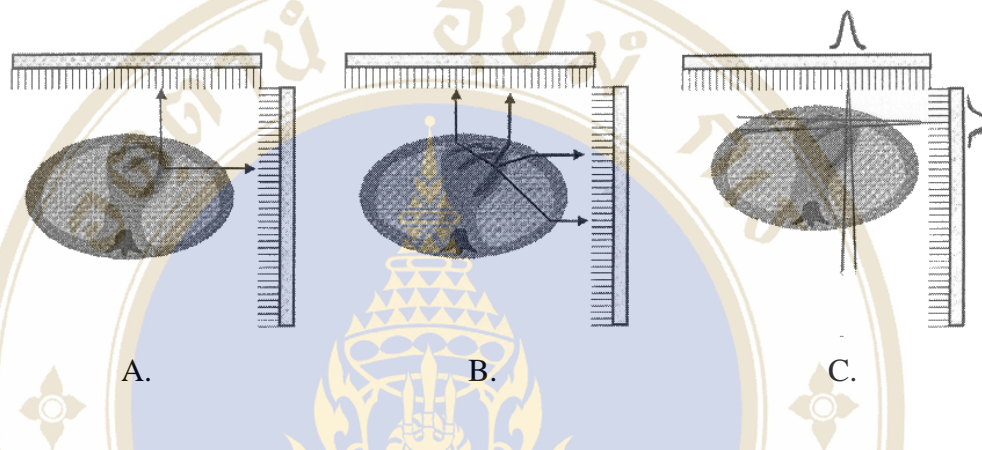


**Figure 1.** Physical factors that compromise SPECT are as follow: A. non-uniform attenuation, B. Compton scatter, and C. varying resolution.

### 1.1 Photon scatter

Photon scatter has long been recognized as contributing to reduce contrast resolution and quantitation errors in cardiac SPECT (5). Scatter can occur via several mechanisms in nuclear medicine, but typically only the Compton interaction is important to SPECT imaging (8). The Compton interaction is characterized by a change in direction and energy loss by a photon as it interacts with orbital electrons in the surrounding tissue. The loss of directional information leads to the inaccurate radiation counts that perform the projection image, which are backprojection along lines that do not intersect the true site of emission (Figure 1B).

A measure of a SPECT system ability to detect scattered photon is the detector energy resolution, which is commonly obtained as the full width at half maximum (FWHM) of the energy spectrum profile, and expressed as a percentage of the photopeak energy. For most systems it is approximately 8 percent to 12 percent for the 140 keV photopeak energy of Tc-99m, which do not permit sufficient energy

discrimination between total scatter rejection, and yield images of less than optimal quality. The shape of the photon energy spectrum reflects the energy loss of scattered photon in tissue by a characteristic broadening and spreading toward lower energy values. Off-peak imaging can be performed by shifting the energy window forward so that the center is above 140 keV, which is used for reducing the relative number of scattered photons under the photopeak. In Compton interaction, the energy loss changes slowly with increasing angle (8). The small-angle scatter is the most abundant in the photopeak window for the common radionuclide, and is therefore the most difficult to detect. Photons may also be scattered by such a sufficiently large angle that they are never detected. In this case, projection values are underestimated, leading to quantitative errors in the SPECT image. The proportion of scattering increase with source depth, and images of sources deeper in body will be more degraded than more shallow sources.

### 1.2 Detector Response

The most important factors in the spatial resolution of images made with a scintillation camera are the geometry of the collimator and the distance from the camera face. The resolution of both fan beam and parallel hole collimators degrades with distance. This effect is shown with a parallel hole collimator in Figure 1C. As the camera orbits the patient for a circular acquisition, the center of rotation maintains the same distance from the collimator. Because the spatial resolution at any given point in SPECT image is a result of the resolution in each of the planar projections, the center of rotation is the only point in the reconstructed image with symmetric resolution. Reconstructed images from the 180 degree data are known to include a slight distortion in transverse images, caused by variable spatial resolution with depth and non-uniform attenuation (10, 11). These effects are reduced in 360 degree acquisition, in which opposing views are combined by the arithmetic or geometric mean during the reconstruction process. This averages variation in spatial resolution and yields a more uniform resolution response across the reconstruction plan (12).

### 1.3 Photon Attenuation

Absorbed photons via the photoelectric effect in tissue deposited all of their energies and were undetected. An example of the attenuation process in myocardial SPECT is shown in Figure 1A. A photon emitted from the heart and picked up by the detector in an anterior view has traversed a relatively small amount of tissue (soft tissue and bone). In a lateral view, photons must traverse a greater distance but through different materials (including lung) to reach the detector. As the detector moves around the patient, the projection profile varies with the attenuation along the projection ray and the distance to the collimator.

Attenuation is described quantitatively by the linear attenuation coefficient. The process of attenuation is described by

$$A_x = A_0 e^{-\mu x} \quad (1)$$

Where  $A_x$  is the activity measured after attenuation through a thickness of tissues  $x$  and  $A_0$  is the true activity at a point in the body (8). Thus the term  $e^{-\mu x}$  represent the fraction of photons that are attenuated over a distance  $x$ .

The absorption probability increases as photon energy decreases thus attenuation artifacts are reported to be more severe with Tl-201 agent than with Tc-99m (8, 9). The most frequently noted effects of attenuation in myocardial SPECT are artifacts associated with breast attenuation in women and diaphragmatic attenuation in men (8, 9, and 10). Breast attenuation artifacts are commonly identified as a region of decreased count density over the anterior myocardial wall. If the breast position is the same between scan, the appearance of a “fixed” perfusion defect may result and may be interpreted as scar or partial reversibility (ischemia). A breast that is not in the same position between rest and stress scans may masquerade as a reversible defect. Similar changes in apparent perfusion patterns in the inferior myocardial wall were resulting from differences in diaphragmatic attenuation between resting and stress scans. This results in attenuation artifacts, which remain a significant obstacle in the interpretation and quantitation of cardiac SPECT images (4).

### 1.3 X-Ray Transmission Scanning

Attenuation maps generated for attenuation of radionuclide image have been traditionally obtained by using an external radionuclide source. This process is identical conceptually to the process of generating a CT image with an x-ray tube that transmits radiation through the body, with the transmitted intensity recorded by an array of detector elements. The transmission data can then be reconstructed using a tomographic algorithm that inherently calculates the attenuation coefficient at each point in the reconstructed slice. In clinical use, the CT image is represented in terms in terms of normalized CT number or Hounsfield units, name after Godfrey Hounsfield, one of the early pioneers of CT. Nevertheless, the CT image contains pixel values that are related to the linear attenuation coefficient ( $\mu$ ) at that particle point in the patient, calculated for the mean energy of the x-ray photon used to generate the CT image.

### 1.4 CT Reconstruction

Computed Tomography or CT reconstruction uses the transmission measurements which have been taken around the patient to reconstruct cross sectional images in which each pixel represents the attenuation of the corresponding object. The attenuation is represented on an expanded scale where the CT number of a particular material, CT [*material*], is computed with reference to the linear attenuation coefficients of water and air:

$$CT[\text{material}] = 1000 \times \frac{\{\mu[\text{material}] - \mu[\text{water}]\}}{\{\mu[\text{water}] - \mu[\text{air}]\}} \quad (2)$$

Where the linear attenuation value  $\mu[\text{material}]$  depends on the density and atomic number of the material as well as the effective energy of the X-ray beam. On the CT scale, water should have a CT number of 0; and air has a CT number of -1000. This expanded scale gives sufficient range of CT numbers to differentiate body tissues such as muscle, fat and organ tissues with similar attenuation coefficients.

### 1.5 Attenuation Correction of Nuclear images

When the X-ray image is used in the attenuation correction of nuclear images, the attenuation coefficients will be constructed from the CT numbers by using the HV setting to look up the bone and water scaling factors from the attenuation scaling table. Depending on the CT value, there are two formulas used for correcting the attenuation values.

For CT values less than 0, materials are assumed to have energy dependence similar to water and the attenuation values at the required energy keV is obtained as follow:

$$\mu[\text{material, keV}] = \mu[\text{water, keV}] + \frac{\{\mu[\text{water, keV}] - \mu[\text{air, keV}]\} \times \text{CT}}{1000} \quad (3)$$

The conversion factor can be calculated using tables of the linear attenuation values (attenuation per mm) for air and water tabulated at 1 keV intervals up to 511 keV. The application software which performs the attenuation correction converts the attenuation values from per mm to per pixel as required. This conversion does require knowledge of the energy of the target radionuclide to be corrected for CT values above are treated as being a mixture of bone and water and the attenuation values are converted from measurements at the X-ray effective energy,  $kV_{eff}$ , to attenuation values at the required energy keV as follows:

$$\mu[\text{material, keV}] = \mu[\text{water, keV}] + \frac{\text{CT}[\text{HV}] \times \mu[\text{water, kVeff}] \times \{\mu[\text{bone, keV}] - \mu[\text{water, keV}]\}}{1000 \times \{\mu[\text{bone, kVeff}] - \mu[\text{water, kVeff}]\}} \quad (4)$$

## CHAPTER II

### OBJECTIVES

The objectives of the study are as follow:

- 2.1 To evaluate the effects of attenuation correction in myocardial perfusion SPECT.
- 2.2 To compare the cardiac image quality using attenuation correction with the non-correction image.
- 2.3 To evaluate homogeneity of count distribution on myocardial perfusion SPECT images.
- 2.4 To compare sensitivity, specificity and accuracy in myocardial perfusion SPECT images.

## CHAPTER III

### LITERATURE REVIEWS

#### 3.1 Ischemia Heart Disease

Myocardial ischemia occurs when there is an imbalance between the supply of oxygen and the myocardial demand. The causes of ischemic heart disease consist of three main categories; coronary artery disease due to mechanical obstruction of the coronary arteries by atheroma, thrombosis, embolus, spasm. The other cause is decreased in flow of oxygenated blood to the myocardial due to anemia, carboxyhemoglobinemia, and hypotension. An increased in demand for oxygen may contribute to ischemia heart disease such as myocardial hypertrophy.

Coronary artery disease is the major cause of ischemia heart disease. It results from coronary atherosclerosis. Coronary atherosclerosis is a complex process characterized by the accumulation of lipid, macrophages and smooth muscle cells in intimal plaques in the large and medium-sized epicardial coronary arteries. A 50 % reduction in luminal diameter (producing a reduction in luminal cross-section area of approximately 70 %) cause a hemodynamically significant stenosis. At this point the smaller distal intramyocardial arteries and arterioles are maximally dilated, coronary flow reserve is near zero, and any increased in oxygen demand provoked ischemia and results in the patient symptom of angina pectoris. If the stenosis is progressed or suddenly becomes total occlusion, myocardial infarction can occur, which may lead to severe chest pain or death.

Most myocardial infarcts are due to the information of an occlusive coronary artery thrombus at the site of atherosclerotic plaque. The results of acute myocardial infarction usually bring about the biochemical and mechanical changes that impair systolic contraction, decrease myocardial compliance, and predisposition to dangerous arrhythmias.

### **3.2 Diagnosis of Coronary Artery Disease (CAD)**

#### **3.2.1 Electrocardiogram (ECG)**

Electrocardiography is the process of recording the potential changes at the skin surface resulting from depolarization and repolarization of the heart muscle. The record itself is called electrocardiogram (ECG). ECG is the most widely used method to investigate myocardial ischemia, especially in association with exercise stress testing. The advantages of this method are its availability and relatively low cost. However, it suffers from poor sensitivity, specificity and provides only limited information regarding the localization and extent of disease.

#### **3.2.2 Echocardiogram**

Echocardiography uses pulse reflected ultrasound, providing tomographic images of cardiac structures and blood flow, analogous to a thin slice through the heart.

Modern techniques increasingly provide information on myocardial ischemia by detecting regions of hypokinesia or akinesia with the patient either at rest or under stress, for example, when receiving dobutamine.

Evaluation of ventricular systolic function is the most important application of echocardiography. With the degree of left ventricular systolic dysfunction, one can predict clinical outcome for wide ranges of cardiovascular disease, including coronary heart disease, cardiomyopathies, valvular heart disease, and congenital heart disease (22).

#### **3.2.3 Angiography**

Coronary angiography is regarded as the gold standard for diagnosis of coronary artery disease, which reveals the site and extent of coronary artery stenoses. But it provides only limited information on the effects of vascular stenosis on the myocardium, that is, degree and extent of resulting ischemia. The determination of coronary artery lesions by angiography remains largely subjective, although newer techniques employing digitization improve objectivity.

### 3.2.4 Nuclear cardiology

Myocardial Perfusion SPECT is noninvasive testing modalities which widely available during the last three decades. The development of technology in this field allows for the measurement of both myocardial function and relative perfusion at rest and stress. Improvement in perfusion tracers, scintillation cameras, and computer system provides accurate assessment of patients' data in patient with know as well as suspected CAD. A lot of investigator had done vast majority to document the value of the technique in the diagnosis and evaluation of patients with CAD.

## 3.3 Nuclear Cardiology Procedure

### 3.3.1 Principle of Myocardial perfusion SPECT

Gamma rays emitted by the myocardium were detected from many different projections by SPECT detector. Most cardiac SPECT studies acquired with 180-degree arc from the 45-degree right anterior oblique (RAO) view to the 45-degree left posterior oblique (LPO) view. Projection images of the heart from the opposite 180 degrees have poor spatial resolution and contrast due to greater distance and attenuation. The orbits of rotation can either circulation or non circulation (elliptical). High resolution collimator is generally used.

### 3.3.2 Myocardial perfusion radiopharmaceuticals

Thallium-201 (Tl-201) and Technetium-99m-methoxyisobutyl-isonitrile (Tc-99m MIBI) were used as radiopharmaceutical for myocardial perfusion imaging.

#### A) Tl-201

Tl-201 is a potassium analogue to active transport through the plasmatic membrane by means of the Na-K-ATPase pump. After intravenous administration, the kinetics of Tl-201 can be divided into phases; initial uptake and redistribution (9). One of the principal advantages of Tl-201 for myocardial perfusion imaging is its high extraction fraction during transit through the myocardial capillary. The extraction is proportional to relative regional perfusion.

Blood clearance after intravenous injection of Tl-201 is rapid. Peak uptake in the myocardium is 10 to 20 minutes after injection. After initial uptake, Tl-201 leaves the myocardium and is partially replaced by circulating Tl-201 from the

systemic pool, which is also undergoing constant recirculation and redistribution. Thus several hours after initial tracer administration the scintigraphic images depict an equilibrated pattern (24).

#### B) Tc-99m -MIBI

Tc-99m –MIBI is isonitrile lipophilic complex with a positive charge, structurally it contains six-isonitrile component around the central Tc-99m atom. Tc-99m has a half life of six hours and emits monoenergetic gamma rays at 140 KeV. In contrast to Tl-201, the cardiac membrane transport of Tc-99m-MIBI is passive. Because of the physical characteristics of Tc-99m, larger dose of Tc-99m-MIBI is used than with Tl-201, usually in the range of 30 mCi, resulting in improved images. Following its extraction from the blood, Tc-99m-MIBI is bound by mitochondria with only a limited amount of myocardial washout (25-26). The initial uptake of Tc-99m-MIBI is a function of myocardial perfusion to viable tissue as Tl-201.

#### 3.3.3 Image acquisition

SPECT detector rotates to different position around the patient and acquires an image at each angle. The rotation can either be in a continuous or step and shoot mode. Acquisition matrix size could either be 64 x 64 or 128 x 128. Using too few projections create radial streak artifacts in the reconstructed transverse images.

##### 3.3.3.1 Single Photon Emission Computed Tomography (SPECT)/CT

Single Photon Emission Computed Tomography (SPECT) is one of several medical imaging techniques provide with superior quality than planar images. As SPECT provides the three-dimensional images, the positions of distributed radioactive tracers injected, inhaled or ingested by the patient are displayed after the processing several projections around the patient. The radioactive tracers will be accumulated at the target organ by biological mechanism. SPECT provides high-contrast images of the three-dimensional distribution of internally distributed radiopharmaceuticals. These images not only allow accurate anatomic localization of abnormalities, but also have potential for providing quantitative information about the regional concentrations of radioactivity and its volume of distribution (4).

SPECT consists of two main components; rotating gamma camera and computer. It generates transverse images depicting the distribution of x-ray or gamma ray emitting nuclides in patients. Standard planar projection images are acquired from an arc of 180 degrees (most cardiac SPECT) or 360 degrees (most noncardiac SPECT) about the patient.

Hybrid (SPECT/CT) scanners with the gamma camera gantry moulded to the front of a CT unit so that the patient can be transported into the X-ray beam before or after the SPECT acquisition. Some CT units are of a low resolution design and generate crude, single slice CT images which are sufficient accurate for SPECT attenuation correction but are insufficient quality for diagnostic, as shown in Figure 2.



**Figure 2.** A low resolution CT scan generated for attenuation correction in a SPECT/CT system.

#### 3.3.4 Image Reconstruction

SPECT begins with the acquisition of projection sets that are line integrals or activity profiles measured from many angular views around the patient. There are two main types of algorithm used to reconstruct SPECT images. The first one is based on direct analytical methods using equations that relate to the projection data and the source distribution. The second one consists of iterative step, in which an initial trial solution is modified successively until an acceptable estimation of the source distribution is obtained.

Most SPECT system uses the first type of algorithm, which is based on back-projection of the filtered projections (Bracewell and Riddle, 1967; Ramachandran and Lakshminarayanan, 1971). This method is referred to a filter back-projection (FBP).

### 3.3.4.1 Filter back-projection (11)

The simple back-projection results in a blurred image, with streaks emanating from areas of high activity (This is call the star artifact). This artifact can be eliminated by the underlying mathematics of reconstruction, as was first done by Radon in 1917. The mathematical function describing the reconstruction process contains a filter that is used to modify each projection before back-projection. Conceptually, this filter produces negative side regions around hot areas in each projection during a reconstruction (Figure 3).

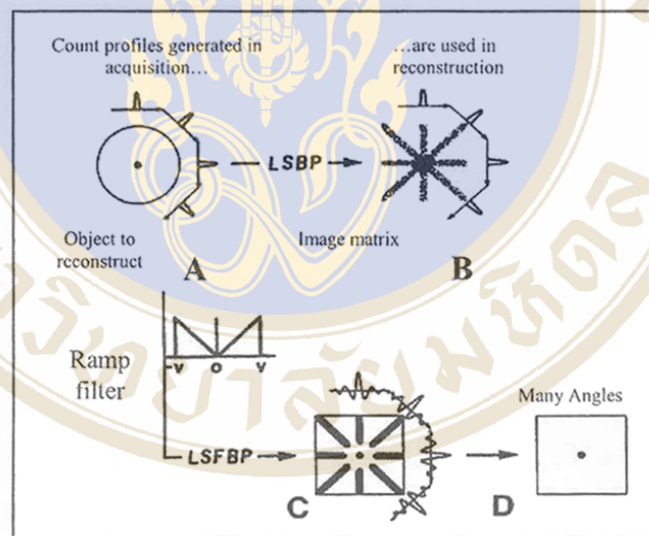


**Figure 3.** Tomographic reconstruction of point source (A), by linear superimposition of back-projection (LSBP) (B), and linear superimposition of filter back-projection (LSFBP) (C and D),  $v$  = frequency (17).

Mathematically, a “perfect” filter exists, called the ramp filter progressively boosts the power of higher and higher spatial frequencies, which are expressed in cycles/distance (Figure 4). High spatial frequencies are generated by the edges of organs and other structures in the patient and by image noise. Thus the ramp filter best preserves spatial resolution but also boosts noise significantly. In general, the filter used in practice are a combination of the ramp filter with a “low-pass” or “smoothing” filter such as Butterworth filter.

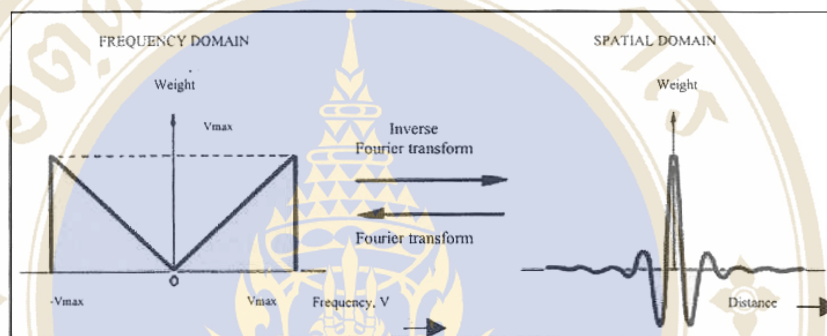


**Figure 4.** Ramp filter in frequency domain (left) and corresponding spatial domain filter (right). Ramp filter is Fourier transform of spatial domain filter, which in turn is inverse Fourier transform of ramp filter (17).

#### 3.3.4.2 Iterative reconstruction (18, 19)

The methods based on spatial frequencies (i.e. filtered back-projection) give use a very efficient method of reconstruction, but they assume that the data are simple projection ray sums. When other effects such as attenuation and scatter are present, these methods are susceptible to creating artifacts. A more general approach is to use an iterative reconstruction. The key to iterative reconstruction is a good understanding of the data collection process. The iterative methods are based on a set of sequential approximations.

The iterative methods start with appropriate initial guess about the reconstructed image. The algorithm then determines what the acquired data would be if that guess were correct. The difference between the guessed parameters is the error. Some types of reconstruction are based on modifications suggested by the errors. The

reconstructed error can be used to correct the guess of the image. So the process takes time and Figure 5 shows the method chart.

The primary advantage of iterative reconstruction over conventional filtered back-projection, is the incorporation of gamma camera imaging physics into the reconstruction model. At the highest level, iterative reconstruction consists of two essential steps. The first step involves calculating the probability density matrix ( $PDM_i$ ) for each voxel  $F_i$  within the object distribution volume. Each data point  $D_{ij}$  in the  $PDM_i$  represents the probability ( $\geq 0$ ) that the radioactivity at voxel  $F_i$  will be detected in pixel  $P_j$  in the projection set (on the other hand, the probability that an event detected in pixel  $P_j$  originated at voxel  $F_i$ ). Each  $D_{ij}$  in each  $PDM_i$  is typically calculated by using both attenuation maps and/or resolution functions. The second step involves calculation of an initial estimate of the reconstructed slice (such as a traditional filter back-projection), following by repeating, or iterative, execution of the projection/back-projection process using the  $PDM_s$  until either a stopping criteria or a desired number of iterations has been reached.

The iterative projection/back-projection process is illustrated in Figure 6. The current estimate of the reconstructed slice,  $F_{est}$ , is projected by using the PDM, creating an estimate projection set,  $P_{est}$ . The current  $P_{est}$  is then either subtracted from or divided into the original projection set,  $P$ , to form an error projection set,  $e_{proj}$ . The original  $P$  may be smoothed, or regularized, first, to reduce the effect to Poisson statistical noise. The  $e_{proj}$  is then backprojected by using an algebraic combination of the PDM and its transpose (rows and columns interchanging), producing an error reconstruction,  $err_{est}$ . The  $err_{est}$  is multiplied by a scale factor,  $r$  (between 0 and 1), to reduce oscillation in the iterative process, and is then either added to or multiplied by the current  $F_{est}$  to produce a new  $F_{est}$ . The iteration cycle is then repeated.

The first iterative techniques applied to SPECT were based on the MLEM algorithm (maximum-likelihood expectation maximization). However, such an algorithm is extremely computer intensive, and requires many iterations to arrive at a good estimation. In recent years, an algorithm known as ordered-subset EM (OSEM) has emerged as an efficient alternative, by using only a subset of the entire projection set in each back-projection step. OSEM greatly reduces the number of iterations required, providing iterative reconstructions in a clinically acceptable timeframe

(within several minutes or less for an entire SPECT volume). Thus, OSEM has become the current method of choice for commercial implementation.

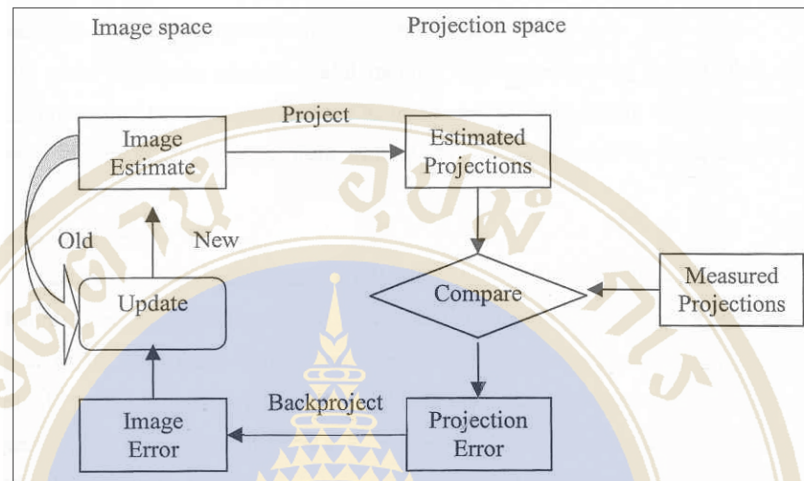


**Figure 5.** Flowchart of iterative method.

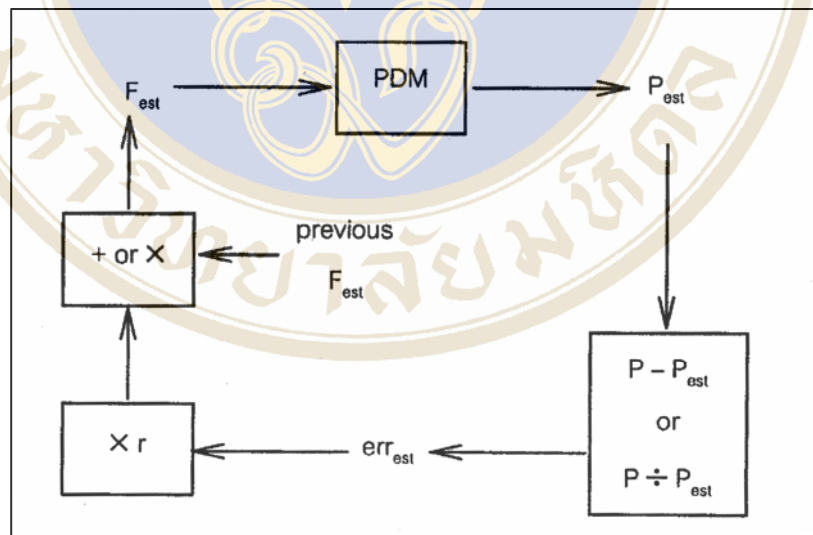


**Figure 6.** Graphical representation of the iterative reconstruction process. (from Distance Assisted Training Programme for Nuclear Medicine Technologists).

### 3.3.5 Image Filtering

Ramp filter is used for removing the blurring caused by the simple back – projection. At the same time however, the ramp also greatly amplifies the noise within the projections. The quality of clinical images is seriously degraded because of the presence of excessive noise in the reconstructed images.

In order to obtain clinical useful images, it is necessary to further filter the projections before the back-projection. The additional filtering should remove some of the noise by smoothing the projections without altering the effect of the ramp filter.

#### 3.3.5.1 Fourier Transform (18)

A sine wave (Figure 7) can be fully described by its frequency (the number of oscillations per unit of distance) and amplitude (The height of the oscillating curve). Thus a single sine wave can be represented as a single point when plotted on amplitude versus frequency axes Figure 8. Suppose that we have a different curve (Figure 8A) that is performed by adding together three different sine waves (Figure 8B). These can be plotted on the amplitude versus frequency axes (Figure 8C) which has identical meaning to the original curve providing that the original curve is the sum of sine waves of various frequencies weighted by the amplitudes as represented as the Fourier plot.

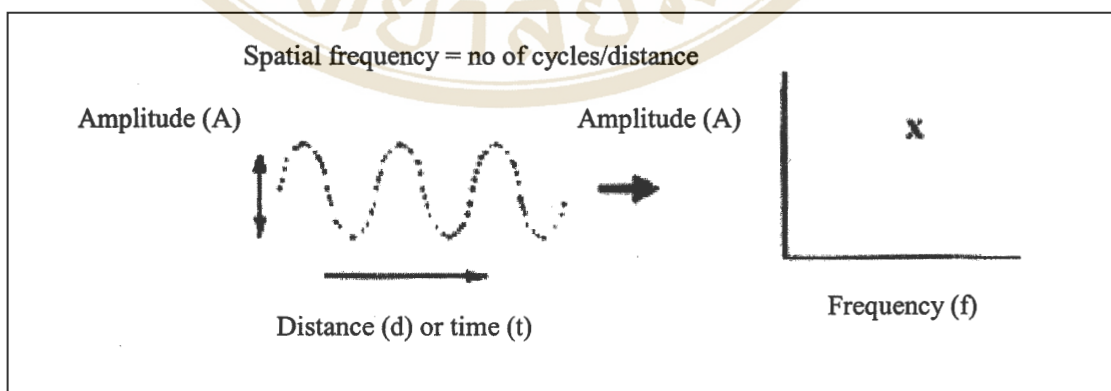


**Figure 7.** An alternative way to draw a sine wave (from Distance Assisted Training Programme for Nuclear Medicine Technologists).

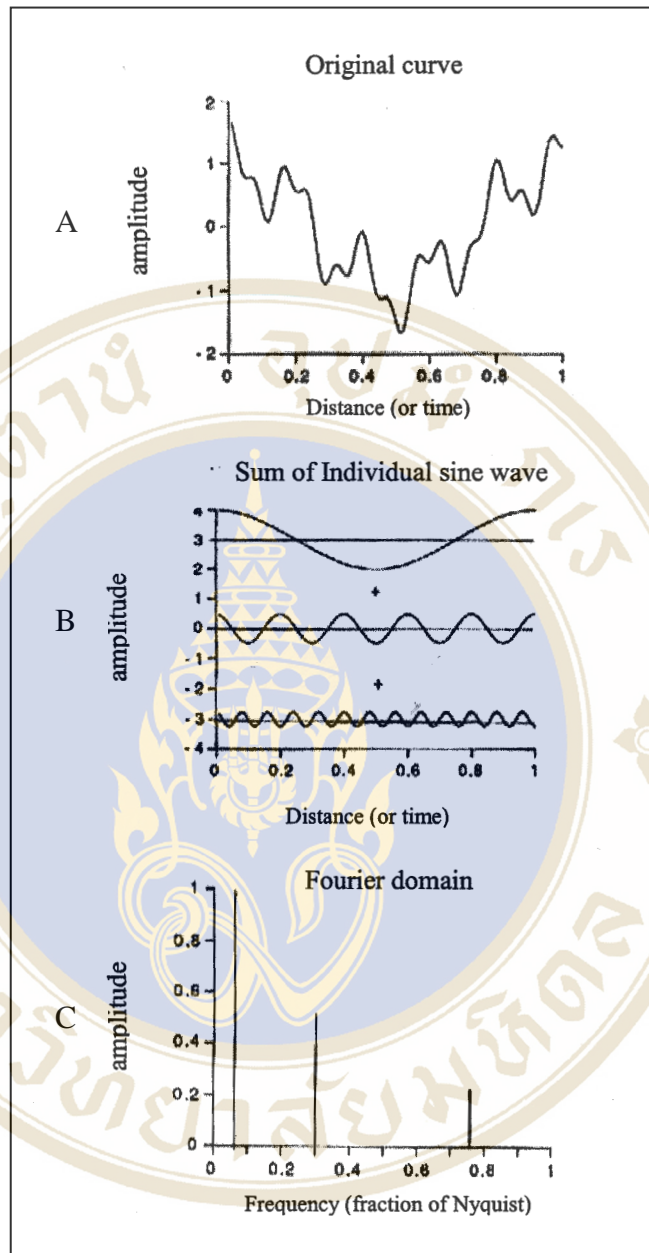


**Figure 8.** The Fourier transform: the function represented in (A) consisting of the sum three sine waves of different frequencies and amplitude also (B). They can be plotted on an alternative set of axes: amplitude versus frequency (C). Such the plot is the Fourier transform of the original curve, which simply illustrated those frequencies that weighted by the respective amplitudes, sum to provide the original curve.

Practically, the function required to transform data for this alternative set of axes is the Fourier transform (FT). The FT simply provides an alternative means of describing the data. Note that the FT of a two-dimensional image also has two dimensions. Typically, the FT of a continuous curve has a continuum of frequencies represented, rather than the discrete ones. Frequency will have units of 1/time in the case of a time-activity curve or will involve units of 1/distance (spatial frequency) in the case of an image.

The inverse FT provides an exact reverse process which simply transforms the data back to the normal activity-time (or distance) axes.

#### 3.3.5.2 Frequency unit

The unit of frequency is in the different forms such as cycles per cm, cycles per pixel or cycles per length of the gamma camera. If the camera field size is 400 mm and matrix size is 32×32 then, in this case, the same frequency as illustrated in Figure 9 can be written as:

Since 16 cycles occupy the camera field of view, the unit is 16 cycle per camera field of view.

OR, given 32 pixels occupy the field of view, containing 16 cycles; the unit is 0.5 cycles per pixel.

OR, given 1 pixel measures  $40/32$  cm = 1.25 cm, then unit is 0.4 cycles per pixel.

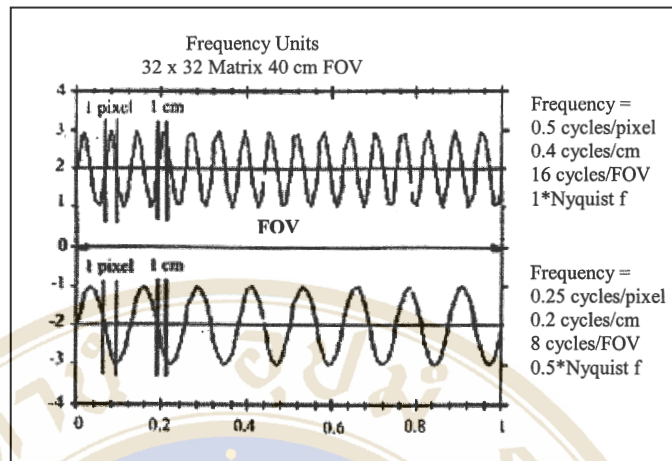


**Figure 9.** Unit for representing frequency (from Distance Assisted Training Programme for Nuclear Medicine Technologists).

### 3.3.5.3 Nyquist frequency

In order to adequately preserve a particular frequency in a digital image (or curve), the data must have sufficient sampling. The sampling theorem states that there must be more than two digital samples (measured values or pixels) per cycle of that particular frequency otherwise the frequency will not be accurately preserved. The Nyquist frequency ( $f_N$ ) is defined as the maximum frequency which could be recovered with a particular matrix size [ $f_N = 1/(2 \times \text{pixel size})$ ]. Such the definition providing the adequately sampled image, the Nyquist frequency will typically be larger than any frequency in the image.

### 3.3.5.4 Ramp Filter

The ramp filter removes the effect of the blurring due to simple back projection. Such the filter has a very simple shape in the frequency domain: its gain increases linearly with frequency (Figure 10). It was defined in the frequency domain as follow:

$$H(F) = |f|$$

Where  $f$  is the frequency

The frequency spectrum of the projection is the sum of the object spectrum and that of the noise. At the lower frequencies the object spectrum dominates while at the

higher frequencies the noise is dominant. Thus the ramp filter, while removing the blur due to the back projection, also increases the noise in the reconstructed image especially at high frequencies. With clinical images, it is necessary to remove the excessive noise by additional filtering. The noise reduction can be achieved by multiplying the ramp filter in the frequency domain by a second filter most often known as a “window”.

$$\text{Back projection filter} = \text{ramp} \times \text{window}$$

$$H(F) = |f|W(f)$$

where  $W(f)$  is the modulation transfer function of the window.

The modulation transfer function of the windows used in SPECT imaging is such that it attenuates greatly at high frequencies where mostly noise is present while preserving the lower frequencies where the object spectrum dominates. The application of a window results in a smoother (loss resolution) and less noisy reconstruction image. The use of a window is therefore a compromise between noise reduction and loss of resolution.

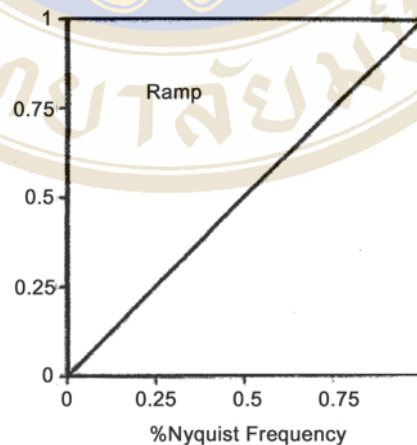


**Figure 10.** A plot of a ramp filter in frequency space.

### 3.3.5.5 Butterworth filter (32).

The most popular low-pass filters used in nuclear cardiology belong to the Hanning and the Butterworth families. Traditionally, Hanning filters were used to process  $^{201}\text{Tl}$  images whereas Butterworth filters were preferred for  $^{99\text{m}}\text{Tc}$  images, but the flexibility and ease of design of Butterworth filters have made them the filters of choice in most nuclear medicine procedures today.

A Butterworth filter in the frequency ( $f$ ) domain is shaped like a curve described by the equation:

$$\text{Butterworth}(f) = \frac{1}{1 + \left(\frac{f}{f_c}\right)^{2n}}$$

where  $f_c$  is the critical, or cutoff, frequency and  $n$  is the order of the filter. From simple mathematic considerations, it is apparent that any Butterworth filter has amplitude 1 when  $f$  is small (low frequencies), amplitude 0 when  $f$  is large (high frequencies), and amplitude 0.5 when  $f$  equals  $f_c$ . However, the mode of transition from 1 to 0 can be profoundly altered by acting on parameters  $n$  and  $f_c$  of the filter. Essentially, the order of a Butterworth filter controls the slope of the transition, and the critical frequency controls the location of the middle point of the slope (Fig. 11). One should be aware that some confusion exists as to the units of measurement for the critical frequency of a Butterworth filter. Although some individuals prefer to express the critical frequency as a 0–1 numeric range, with 1 being the highest attainable frequency, or 100% of the Nyquist frequency, others point out that the Nyquist frequency is, by definition, equivalent to 0.5 cycles per pixel and adopt a 0–0.5 range instead. In other words, the same critical frequency can be reported as 0.3 or 0.6 on 2 different camera systems. In any event, whether a critical frequency is expressed in cycles per pixel or as a fraction of the Nyquist frequency, any measurement expressed in frequency terms must, clearly, always be accompanied by knowledge of the pixel size.

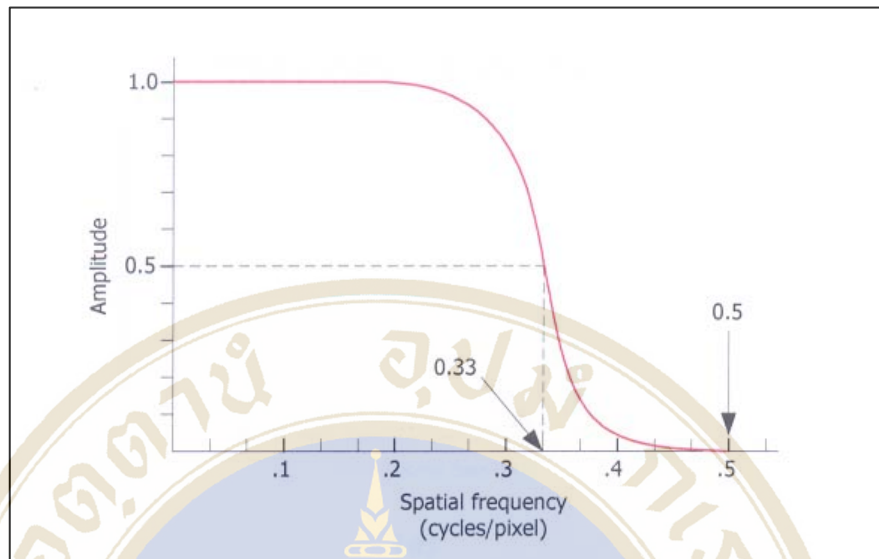


**Figure 11.** Butterworth filter with parameters  $n = 0.5$  and  $f_c = 0.33$ .

### 3.3.6 Reorientation

Tomographic reconstruction of projection images procedures transaxial images, that is, images perpendicular to the long axis of the patient. Because the orientation of the heart relative to the patient's long axis varies from patient, the transverse tomograms are reoriented into three sets of oblique tomogram (Figure 12 to Figure 16):

- A) Short axes (perpendicular to the long axis of the left ventricle) are displayed from apex to base (Figure 14).
- B) Vertical long axes (parallel to the long axis of the left ventricle in close to a vertical plane) are displayed from septal to lateral wall (Figure 15).
- C) Horizontal long axes (parallel to the long axis of the left ventricle in close to a horizontal plane) are displayed from anterior to inferior wall (Figure 16).

The advantages of reorientation including easier visual assessment of myocardial perfusion defects and the ability of performing more accurately quantify and display perfusion parameters.

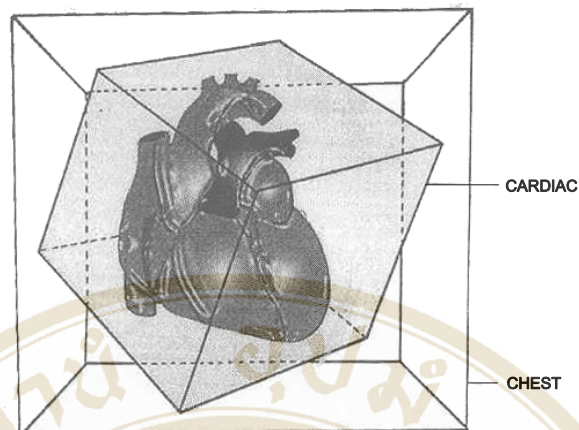


**Figure 12.** If one considered the chest a cube, then the heart is located in its own cube within the large chest cube. The heart (and the heart cube) is pointing downwards, to the left, and anterior. Usually about 45 degree in each direction, but there are considerable individual variations.

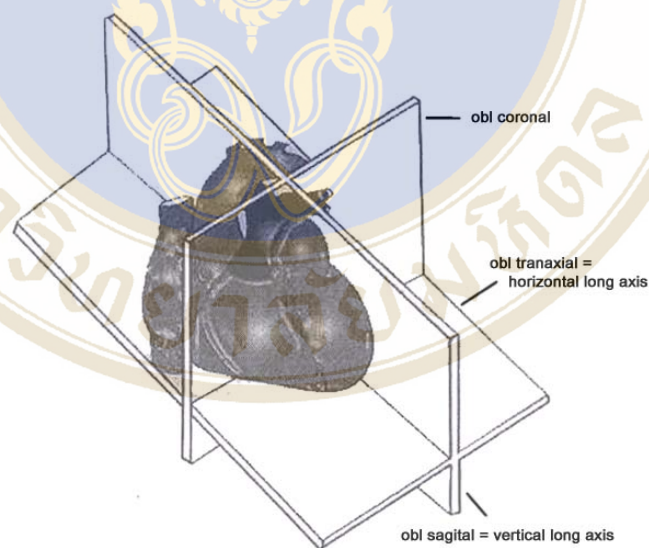


**Figure 13.** Illustration of the reconstructed cuts perpendicular to the long axis (coronal = short axis cuts) and perpendicular to the short axis (sagittal = axis and horizontal = transaxial cuts)

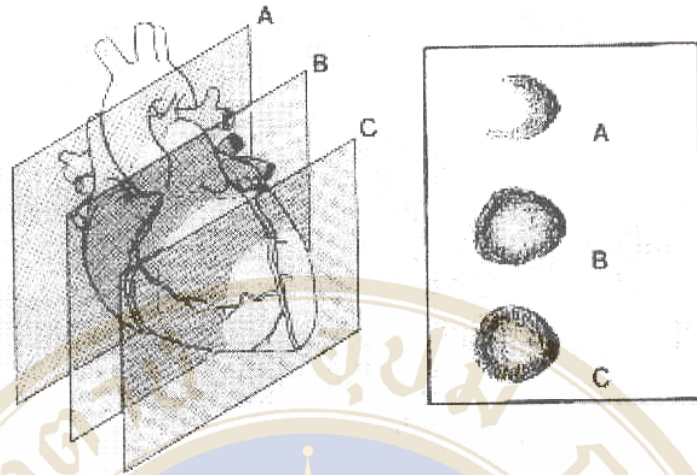


**Figure 14.** Illustration of Short axis slices, from base to apex.

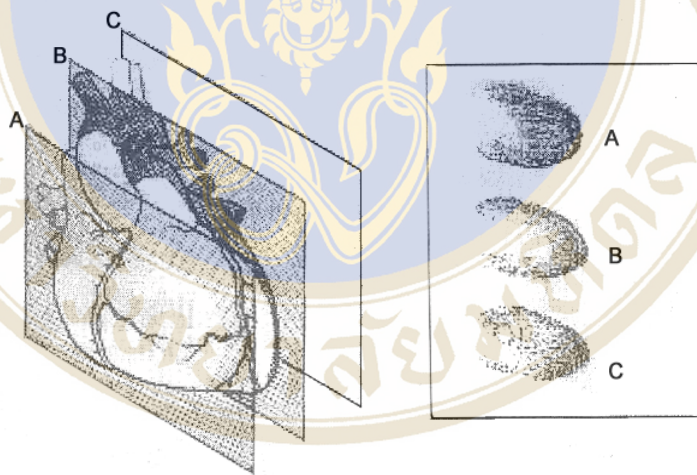


**Figure 15.** Illustration of Vertical long axis, LV septum to free wall.

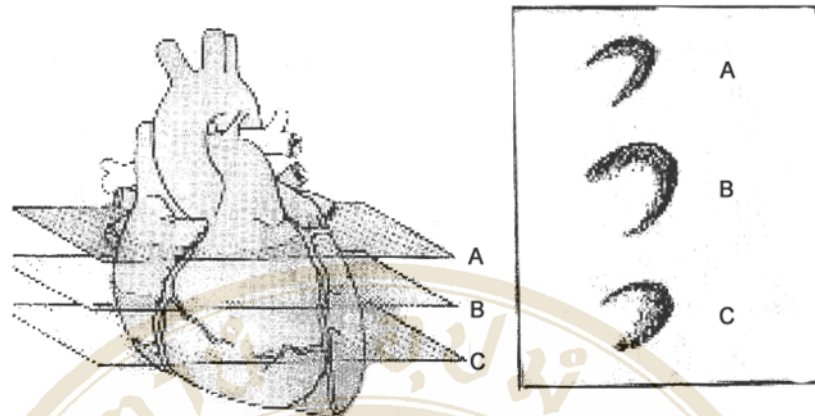


**Figure 16.** Illustration of Horizontal long axis, LV anterior to inferior.

### 3.4 Literature Reviews

In 1996 Edward et al (7) studied the diagnostic performance of attenuation-correction (AC) stress  $^{99m}\text{Tc}$ - sestamibi cardiac SPECT for identification of coronary heart disease (CHD), methods use a  $^{241}\text{Am}$  transmission line source, simultaneous transmission/emission tomography (TCT/ECT), iterative reconstructed AC stress  $^{99m}\text{Tc}$ - sestamibi perfusion images were compared with uncorrected (NC) filter-backprojection images. Normal database polar maps were constructed from AC and NC images for quantitative analyses. From the low-likelihood patients, the visual and quantitative normally rates increase from 0.88 and 0.76 for NC to 0.98 and 0.95 for AC ( $p < .05$ ). For the detection of CHD, the receiver operating characteristic curves for the AC images demonstrated improved discrimination capacity ( $p < .05$ ), and sensitivity/specificity values increased from 0.78/0.46 (NC) to 0.84/0.82 (AC) with visual analysis and 0.84/0.46 (NC) to 0.88/0.82 (AC) with quantitative analysis.

In 2000 Luis et al (27) determined the improved uniformity in tomographic myocardial perfusion imaging with attenuation correction in men and women. Four imaging protocols were comparing: a  $180^\circ$  acquisition and filtered backprojection reconstruction (FBP), a  $360^\circ$  acquisition and FBP, a  $360^\circ$  acquisition and iterative reconstruction (IT), and a  $360^\circ$  acquisition with IT and AC. The resulted,  $180^\circ$ ,  $360^\circ$  FBP, and  $360^\circ$  IT showed sex differences, with decreased tracer concentration in

anterior wall in women and decrease tracer concentration in inferior wall in men. AC images showed the greatest uniformity (9.9% coefficient of variation for AC versus 12.5% for IT,  $p < 0.0001$ ), and no statistically significant differences in uniformity were seen male and female AC studies.

In 2005 Yasmin et al (28) studies validation of SPECT attenuation correction using x-ray computed tomography derived attenuation maps in phantom AC improved homogeneity from  $11\% \pm 2$  to  $5\% \pm 1\%$ . Normal patient files were created from 37 normal subjects with a low likelihood ( $< 3\%$ ) of CAD and 118 patients of CAD who had stress Technetium 99m sestamibi or tetrofosmin stress SPECT imaging and coronary angiography. SPECT images with and without AC were interpreted by 4 blinded readers with different interpretative attitudes. Results, AC improved the diagnostic performance of all readers, particularly the normalcy rate. The degree of improvement depended on interpretative attitudes.

In 2005 Daisuke et al (27) evaluated the clinical usefulness of X-ray CT base attenuation correction (AC) in patients undergoing myocardial perfusion imaging by comparing their myocardial AC and non corrected (NC) SPECT images with the coronary angiography (CAG). Retrospective reviewed the myocardial SPECT images of 30 patients (18 men, 12 women), 13 patients with coronary artery disease (CAD) and 17 without CAD were confirmed by CAG. Two readers reviewed the myocardial SPECT images compared with AC and NC. A result for AC- images, the observer consensus for analysis was 0.84 for the LAD-, 0.87 for the LCX-, and 0.71 for the RCA-territory. For NC-images, it was 0.91, 0.71, and 0.78. AC resulted in statistically significant improvements in overall diagnostic accuracy (sensitivity/specificity/accuracy = 79% / 93% / 89%, 67% / 86% / 81% respectively, for AC- and NC-images). The specificity, diagnostic accuracy was significantly increased on AC-images.

## CHAPTER IV

### MATERIALS AND METHODS

#### 4.1 Materials

##### 4.1.1 Single Photon Emission Computed Tomography (SPECT/CT) system

SPECT/CT, Model H3000 YM Infinia Hawkeye; GE Medical System, dual head and Xeleris computer software was used as tomographic imaging instrument. The detector head had a large rectangular field of view of 540 mm x 400 mm. Each detector head housed a 9.5 mm thick sodium iodide (NaI (Tl)) crystal and equipped with parallel-hole low-energy high-resolution collimator as shown in Figure 17. CT consisted of an x-ray tube and 383 image array detectors located opposite of each other.



**Figure 17.** SPECT/CT System, Model H3000 YM Infinia Hawkeye.

#### 4.1.2 Anthropomorphic torso phantom<sup>TM</sup> with cardiac insert<sup>TM</sup>

All studies were performed by using a commercial available phantom (Model ECT/TOR/P, Data Spectrum Corporation). The phantom consists of lucite body with many compartments to simulate upper torso of average to large male/female patients (38 x 26 cm) with 9.5 mm wall thickness.

Two lungs filled with Styrofoam<sup>®</sup> beads for left lung and right lung are 0.36 liters and 0.44 liters respectively. Liver is isolated from the other organ with removable filler cap to allow for independent tracer concentration for 1.2 liters volume. Spine (high density Teflon<sup>®</sup>) allows qualitative and quantitative evaluation of attenuation and scatter effects due to vertebrae. Cylinder volume with lung, spine and cardiac insert is 7.4 liters as shown in figure 18.

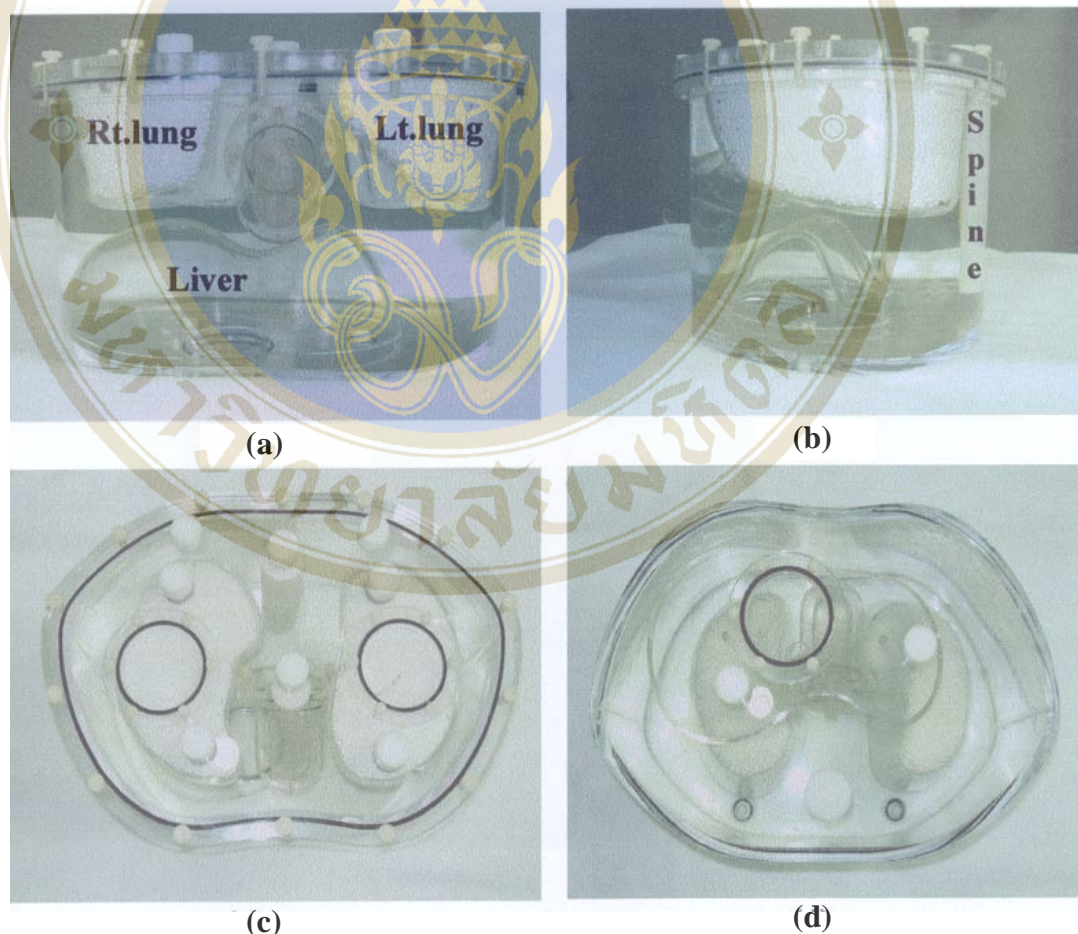


**Figure 18.** The Anthropomorphic phantom Model ECT/TOR/P, (Data Spectrum Corporation) in various view, (a) frontal view, (b) lateral view, (c) top view, and (d) bottom view.

Cardiac insert<sup>TM</sup> ((Model ECT/TOR/I, Data Spectrum Corporation) (Figure 19) simulates normal and abnormal myocardial uptake and radioactivity in left ventricular chamber. Overall length and diameter of ventricle were 9.3 cm and 6.0 cm with 61 ml ventricle volume. Myocardial volume was 110 ml with 1.0 cm wall thickness. The solid defect set with 1.0 cm wall thickness 60° x 2 cm length was used in the study of transmural cold abnormalities of myocardium. The Cardiac insert<sup>TM</sup> were used to evaluate cardiac ECT data acquisition and reconstruction methods, as well as practice diagnosis.

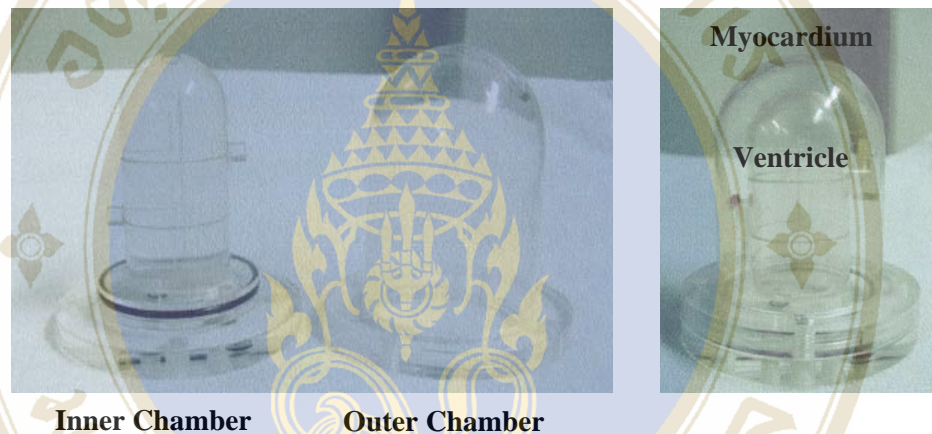


**Figure 19.** The cardiac insert Model ECT/TOR/I, (Data Spectrum Corporation).

#### 4.1.3 Myocardial solid defect sets

The solid defects set consisted two defects with 1.0 cm wall thickness, 60° x 2 cm length and 45° x 1.5 cm lengths. (Figure 20)

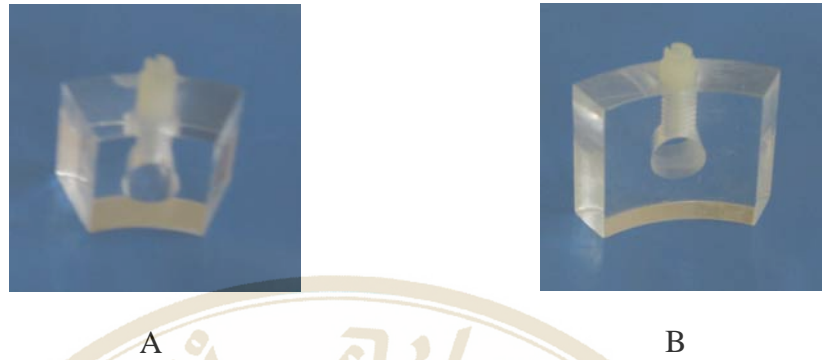


**Figure 20.** Myocardial solid defect sets

- A. The defects with 1.0 cm wall thickness, 60° x 2 cm length
- B. The defects with 1.0 cm wall thickness, 45° x 1.5 cm length

#### 4.1.3 Dose Calibrator

The dose calibrator, Capintec model CRC15R, is a cylindrically shaped well-type ionization chamber, sealed chamber with a central well and filled with argon and traces of halogen at high pressure of about 20 atmospheres (Figure 21). A radioactive source container placed at the axis of the cylinder so that the radioactive source was set close to the center of the ionization chamber.



**Figure 21.** The dose calibrator, Capintec (model CRC15R).

#### 4.1.4 Radionuclide

Tc-99m solution was used for filling in Anthropomorphic Torso Phantom.

#### 4.1.5 Study population

##### 4.1.5.1 Normal Database

The study population consisted of 20 volunteers with a low probability of coronary artery disease as determined by  $^{99m}\text{Tc}$ -MIBI myocardial perfusion SPECT/CT imaging. There were 10 males and 10 females with a mean age of 64.65 years (range 43-85) served as normal database. They had to be healthy without a history or family history of heart disease, had no other major medical disease, non cigarette smokers, absence of abnormalities on physical examination and no ischemic pattern change on resting ECG (right bundle branch block was not exclusion criteria but left bundle branch block was), blood pressure not more than 160/95 mmHg, serum cholesterol not more than 200 mg/dl and no medical therapy, fasting plasma glucose not more than 126 mg/dl. (30)

##### 4.1.5.2 Patients

Retrospective studies in 40 patients with a mean age of 65.21 years (range 53-80) who underwent  $^{99m}\text{Tc}$ -MIBI myocardial perfusion SPECT/CT technique from 2004-2005 at Division of Nuclear Medicine, Department of Radiology, Faculty of Medicine Siriraj Hospital, Mahidol University. All of the patients involvement with the angiogram's report.

#### 4.2 Methods

##### 4.2.1 Phantom preparation

The radioactivity concentration in cardiac insert phantom simulated the patient MIBI biodistribution (31). Data Spectrum's manual recommended to use approximately 235  $\mu\text{Ci}$  of Tc-99m in myocardium chamber. The total activity of Tc-99m, 1.855 mCi, was used in phantom preparation. The detail of activity for each individual organ were shown in Table 1

For study lesion, solid defect 60° with 1.0 cm wall thickness, 0.6 cm x 2 cm length size ~5 cm volume was placed in lateral region into the myocardial compartment to stimulate infarcted myocardium.

**Table 1.** Tc-99m activity distribution in the organ

Organ	Activity (mCi)
body	0.46
myocardium	0.235
liver	1.16
Total activity in phantom	1.855

#### 4.2.2 Patient preparation

A patient should have fasted for at least 4 hours (except for water) before an appointment time. Certain medications ( $\beta$ -blocker and Calcium antagonist) have to be omitted for 48 hours prior to the study. In addition, the patient must avoid food and drinks containing caffeine or caffeine-like compounds (for example, coffee, tea, chocolate and colas) for 24 hour before the test.

#### 4.2.3 One day protocol for myocardial perfusion

##### 4.2.3.1 Rest testing

1. After injected 7mCi Tc-99m MIBI for 20 minutes, the patient was given a light meal (eggnog a glass of milk) to empty the gallbladder and encourage clearance from the liver.

2. One hour after the injection, the patient would be sent to the scan room and his supine was scanned with two arms above the head to perform the SPECT/CT acquisition.

##### 4.2.3.2 Stress testing

1. The ECG equipment was connected to the patient's electrodes and established baseline ECG, heart rate and blood pressure were monitored during test.

2. The patient was stress to the maximum achievable exercise according to a standard treadmill protocol test.

3. Twenty two mCi of  $^{99m}\text{Tc}$ -MIBI was injected at the patient's peak exercise; at the point of chest pain, 90% of predicted maximal heart rate, significant ST-T depression on ECG, of fatigue or dyspnea.

4. Then the patient continued exercise on the treadmill 60 seconds prior to cessation of exercise.

5.  $^{99m}\text{Tc}$ -MIBI would be injected intravenously at the time according to the instruction if pharmacological stress were chosen.

6. One hour after the injection, the patient was brought to the scan room and was scanned supine with two arms above the head to performed the SPECT/CT acquisition

#### **4.2.4 Image Acquisition**

The study used an identical hybrid SPECT/CT dual head gamma camera. Emission data were acquired by use of parallel-hole, low-energy high-resolution collimators, with the patient in the supine position.

Acquisition parameters for SPECT image:

- matrix size of 64 x 64
- zoom 1.3
- angle range 90°
- 180 degree, 60 steps, 25 sec/step from RAO to LPO position
- Energy window 140 keV  $\pm$  20 % window width

Acquisition parameters for CT image:

- slice step 10 mm
- voltage 140 kV
- current 2.5 mA

Immediately after acquisition of SPECT image, CT imaging was performed by using GE Hawkeye system.

#### **4.2.5 Computer processing of myocardial perfusion images**

The SPECT emission image data were reconstructed by using ordered-subsets expectation maximization (OSEM) reconstruction technique with 2 iteration and 10 subsets. The reconstructed stress and rest images were smooth with a 3 dimensional

Butterworth low-pass filter with a critical frequency of 0.52 cycles/cm and order of 10. Subsequently, 1-pixel-thick tomographic slices were generated and displayed as short axial, vertical and horizontal long-axis slice. Attenuation correction was applied to emission data by using transmission data from CT image. No scatter or depth-dependent resolution correction was applied.

#### 4.2.6 Data Analysis

##### Part 1: Study in Anthropomorphic torso phantom

4.2.6.1 Comparison of resolution between using IRNC and IRAC technique from the axial image of cardiac phantom with solid defect. The threshold level of the resolution was varied from 35% to 60%, in 5% increments.

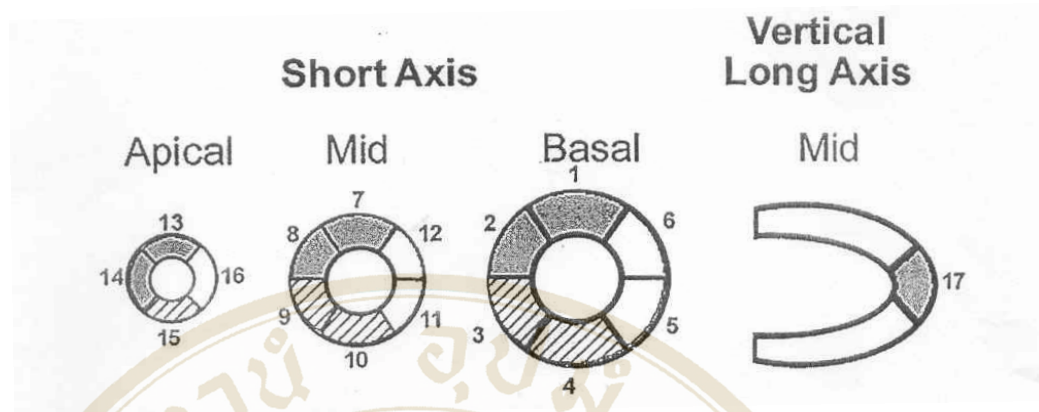
4.2.6.2 Comparison of reconstruction parameters between using IRNC and IRAC technique from the axial image of cardiac phantom with solid defect. The axial image was reconstructed using the iterative OSEM method. The number of subsets was varied from 10 to 40, in 10 subsets increments and varied number of iterations from 1 to 4 iterations in 1 iteration increment.

4.2.6.3 Comparison of percentage of contrast between using IRNC and IRAC technique from the short axis image of cardiac phantom with solid defect. The percentage of contrast was calculated from the minimum count per pixel ( $C_{\min}$ ) and maximum count per pixel ( $C_{\max}$ ) of circumferential profile curve as the equation:

$$\% \text{ contrast} = \frac{C_{\max} - C_{\min}}{C_{\max} + C_{\min}} \times 100$$

4.2.6.4 Comparison of count distribution by using non attenuation correction (IRNC) with attenuation correction (IRAC) technique from polar map image of cardiac phantom without solid defect. The polar map image were created by the normalization count per pixel of 17 regions cardiac segmentations that represented the region of count distribution for myocardial without lesion as shown in Figure 22. The percentage of normalization value is defined as follows:

$$\% \text{ normalization value} = \frac{\text{count per pixel of each region}}{\text{maximum count per pixel of 17 regions}} \times 100$$



- |                        |                       |
|------------------------|-----------------------|
| 1. basal anterior      | 10. mid inferior      |
| 2. basal anteroseptal  | 11. mid inferolateral |
| 3. basal inferoseptal  | 12. mid anterolateral |
| 4. basal inferior      | 13. apical anterior   |
| 5. basal inferolateral | 14. apical septal     |
| 6. basal anterolateral | 15. apical inferior   |
| 7. mid anterior        | 16. apical lateral    |
| 8. mid anteroseptal    | 17. apex              |
| 9. mid inferoseptal    |                       |

**Figure 22.** Diagram of count distribution showing segment observed in the short-axis, vertical long-axis view of myocardium.

## Part 2: Study in patient

4.2.6.5 Comparison of count distribution between using IRNC and IRAC techniques from polar map image of male and female patients with normal myocardium were performed. The percentages of normalization value were calculated from the maximum count per pixel of 17 regions cardiac segmentations. The percentage of normalization value was used to define a uniform index in the myocardium.

4.2.6.6 Comparisons of sensitivity, specificity and accuracy between using IRNC and IRAC technique from short axis images were performed in 40 patients undergoing myocardial perfusion imaging by using the coronary angiography (CAG) as the reference. Myocardial perfusion images were interpreted by two nuclear

medicine physicians who were blind to angiogram results and reconstruction techniques. For quantitative visual analysis an interpretation of each point was done on a five-point scoring system as follow:

- 0 = normal
- 1 = slight reduction of Tc-99m sestamibi uptake
- 2 = moderate reduction of uptake, usually implying significant abnormality
- 3 = severe reduction of uptake
- 4 = absence Tc-99m sestamibi uptake

The sensitivity, specificity and accuracy were calculated from the equation as follow:

$$\text{Sensitivity} = \frac{\text{Number of true positive (TP)}}{\text{Number of true positive(TP) + false negative (FN)}}$$

$$\text{Specificity} = \frac{\text{Number of true negative (TN)}}{\text{Number of true negative(TN) + false negative (FN)}}$$

$$\text{Accuracy} = \frac{\text{Number of true positive (TP) + true negative (TN)}}{\text{Total number of images}}$$

#### 4.3 Statistic Analysis

Statistical evaluation was performed using SPSS software. Continuous data were expressed as mean and standard deviation (SD). Paired 2-sample t-test was used for the difference comparison in normalization count per pixel of 17-region cardiac segment by segment between male patient and female patient images. All statistical test were 2-tailed and a value of  $p < 0.05$  was considered significant. To evaluate quantitative perfusion information, ROC (Receiver Operating Characteristic) curve analysis was applied.

## CHAPTER V

### RESULTS

#### Part 1: Phantom Studies

##### 5.1 Comparison of resolution between using IRNC and IRAC technique from the axial image of cardiac phantom with solid defect.

For the comparisons of resolution, the reconstructed myocardial SPECT images of solid defect phantom by using IRNC and IRAC technique for each threshold level were shown in Figure 23 and Figure 24. The result of area and size of defect between IRNC and IRAC technique for each threshold level are shown in Table 2.

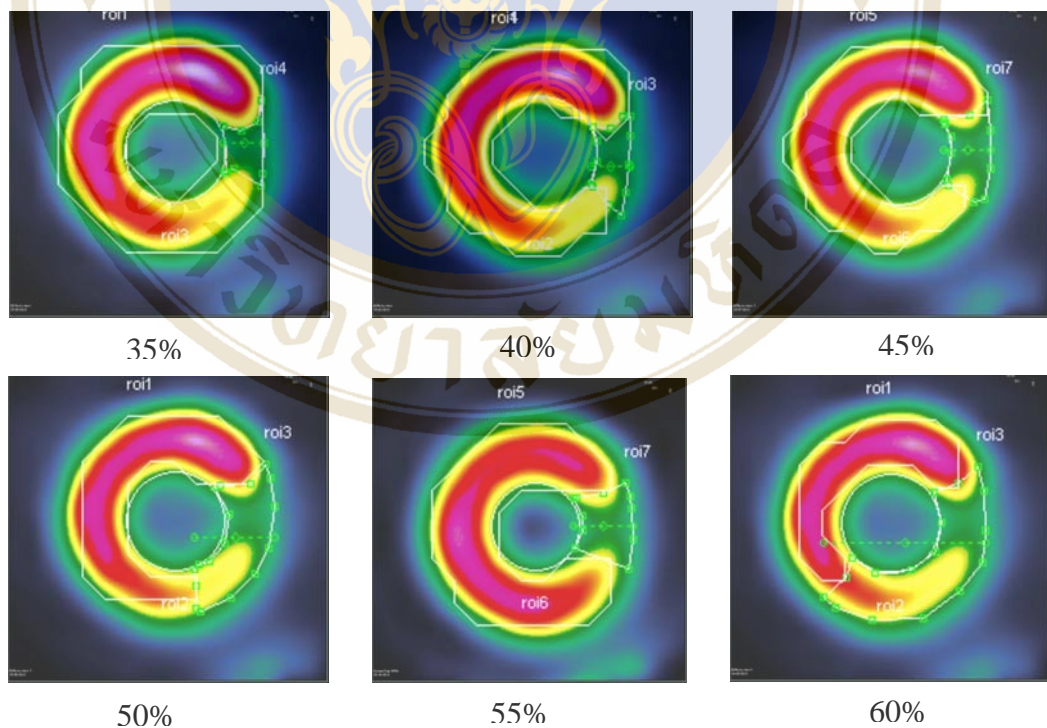


**Figure 23.** The reconstructed myocardial SPECT images of cardiac phantom by using IRNC technique for each threshold level.

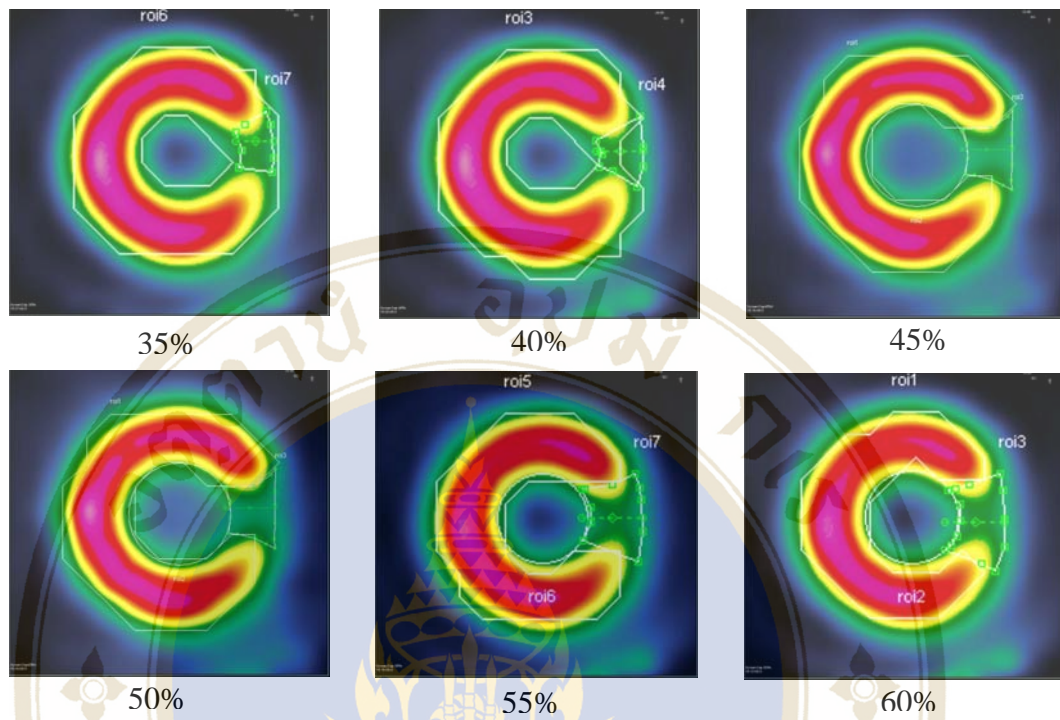


**Figure 24.** The reconstructed myocardial SPECT images of cardiac phantom by using IRAC technique for each threshold level.

**Table 2.** Area and size of defect between IRNC and IRAC myocardial SPECT images for each threshold level.

Threshold level	IRNC		IRAC	
	Area (Pixel)	Size (cm <sup>2</sup> )	Area (Pixel)	Size (cm <sup>2</sup> )
35%	10	3.90	8	3.13
40%	12	4.68	9	3.51
45%	12	4.68	11	4.29
50%	12	4.68	13	5.07
55%	20	7.81	14	5.46
60%	22	8.59	16	6.25

\*Defect size of phantom = 5 cm<sup>2</sup>

From Table 2 it shows that at 50% threshold level of IRAC, the size of defect was almost the same as the phantom defect size of 5 cm<sup>2</sup>.

## 5.2 Comparison of reconstruction parameters between using IRNC and IRAC technique from the axial image of cardiac phantom with solid defect.

For the comparison of reconstruction parameters, the reconstructed myocardial SPECT images of solid defect phantom by using IRNC and IRAC technique for each iteration and number of subset were shown in Figure 25, 26, 27, and 28, respectively. The area and size of defect resulting from IRNC and IRAC technique for each iteration and number of subset are shown in Table 3 and 4, respectively.

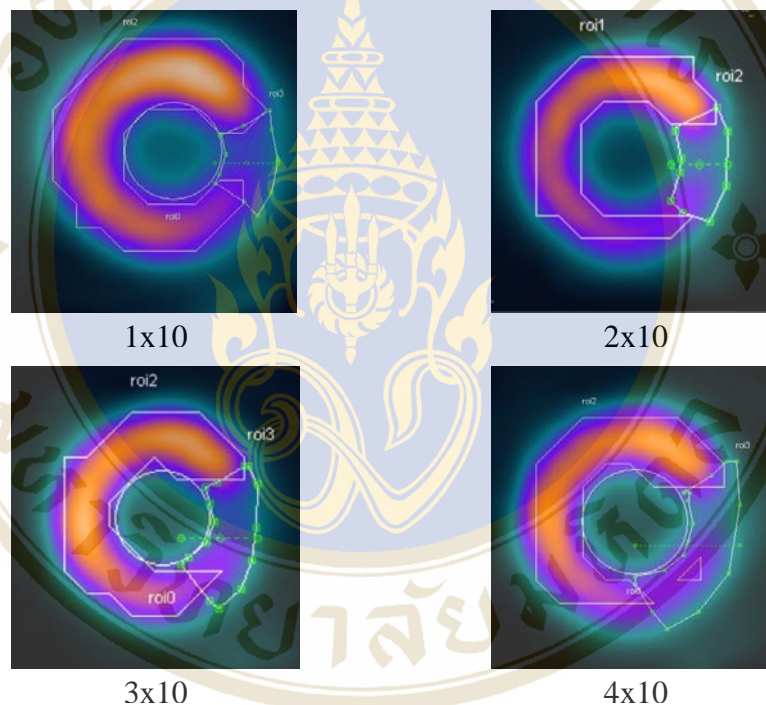


**Figure 25.** The reconstructed myocardial SPECT images of cardiac phantom by using IRNC technique for each iteration with 10 subset.

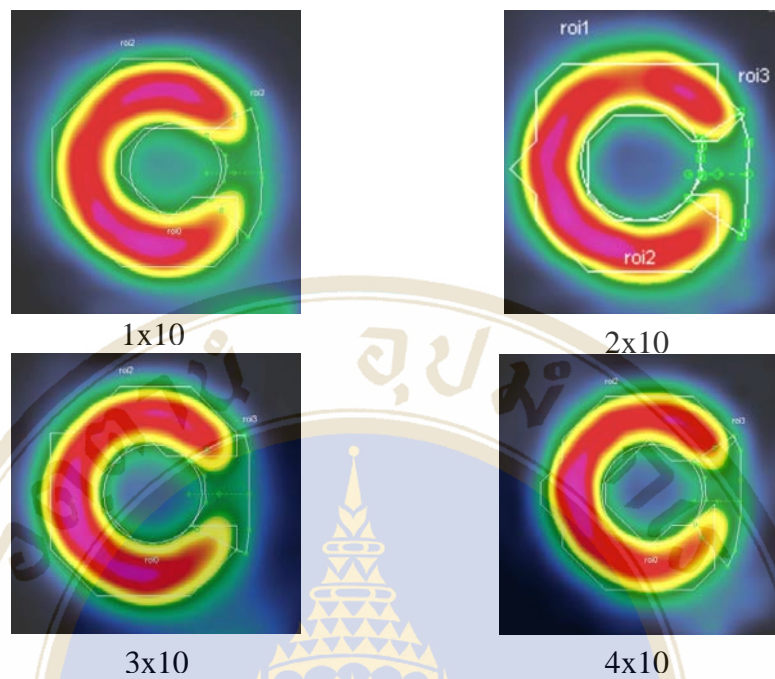


**Figure 26.** The reconstructed myocardial SPECT images of cardiac phantom by using IRAC technique for each iteration with 10 subset.

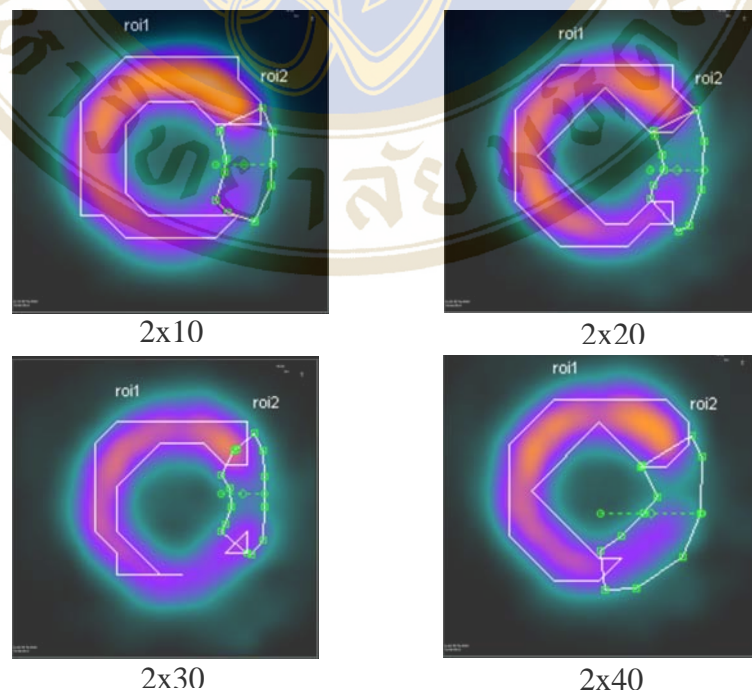


**Figure 27.** The reconstructed myocardial SPECT images of cardiac phantom by using IRNC technique for each number of subset with 2 iteration.

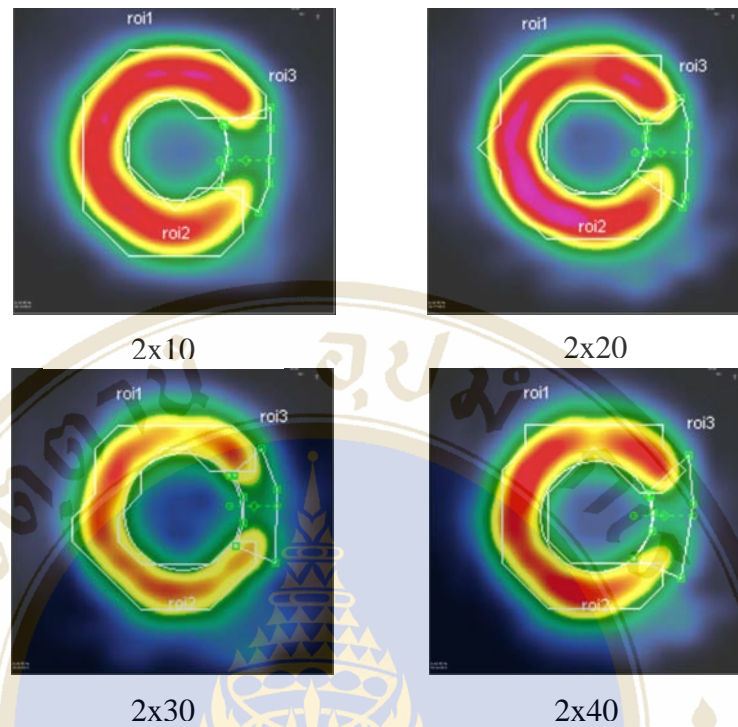


**Figure 28.** The reconstructed myocardial SPECT images of cardiac phantom by using IRAC technique for each number of subset with 2 iteration.

**Table 3.** Area and size of defect between IRNC and IRAC myocardial SPECT images for each iteration.

Numbers of update (iteration x subset)	IRNC		IRAC	
	Area (Pixel)	Size (cm <sup>2</sup> )	Area (Pixel)	Size (cm <sup>2</sup> )
1x10	12	4.68	19	7.42
2x10	18	7.03	13	5.07
3x10	23	8.98	19	7.42
4x10	26	10.10	17	6.64

\*Defect size of phantom = 5 cm<sup>2</sup>

**Table 4.** Area and size of defect between IRNC and IRAC myocardial SPECT images for each number of subset.

Numbers of update (iteration x subset)	IRNC		IRAC	
	Area (Pixel)	Size (cm <sup>2</sup> )	Area (Pixel)	Size (cm <sup>2</sup> )
2x10	18	7.03	13	5.07
2x20	15	5.85	14	5.46
2x30	17	6.64	14	5.46
2x40	26	10.10	14	5.46

\*Defect size of phantom = 5 cm<sup>2</sup>

Table 3 and 4 showed that the number of update of 2 iteration × 10 subset using IRAC technique gave a defect size of the closet value to the phantom defect size of 5 cm<sup>2</sup>. Thus, this number of update was optimum.

### 5.3 Comparison of percentage of contrast between using IRNC and IRAC technique from the short axis image of cardiac phantom with solid defect.

The percentage of contrast resulting from IRNC and IRAC technique applied to myocardial SPECT images of defect phantom studies are shown in Table 5, the graph is shown in Figure 29.

**Table 5.** Percentage contrast of IRNC and IRAC myocardial SPECT images of defect phantom studies.

Myocardial wall	%Contrast		%Difference
	IRNC	IRAC	
Anterior wall	70.75	80.79	12.42
Inferior wall	57.68	75.47	23.57
Lateral wall	80.99	83.38	2.86
Septal wall	62.94	66.73	5.03

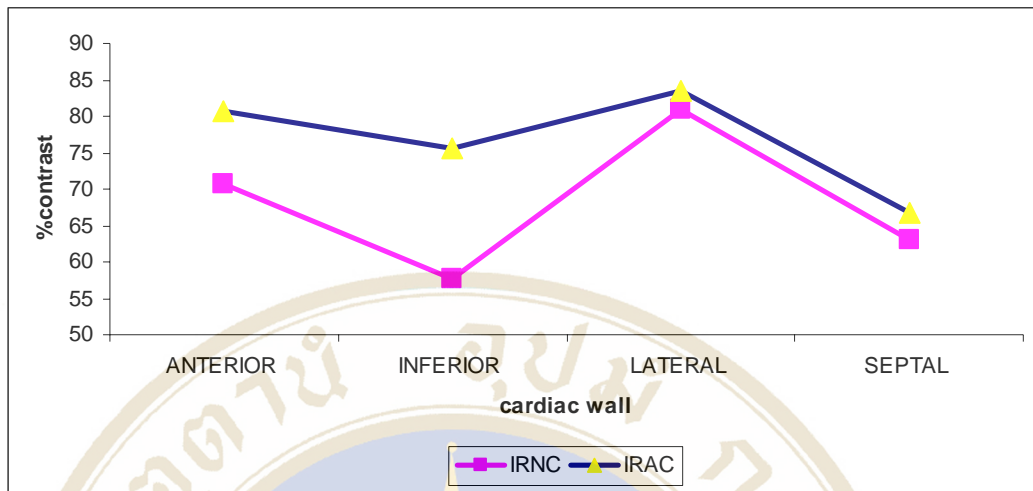


**Figure 29.** The percentage contrast curve of IRNC and IRAC images in phantom studies.

The phantom SPECT images in Figure 30 was clearly shown the IRAC improvement of the activity in anterior, septal, lateral and inferior walls.

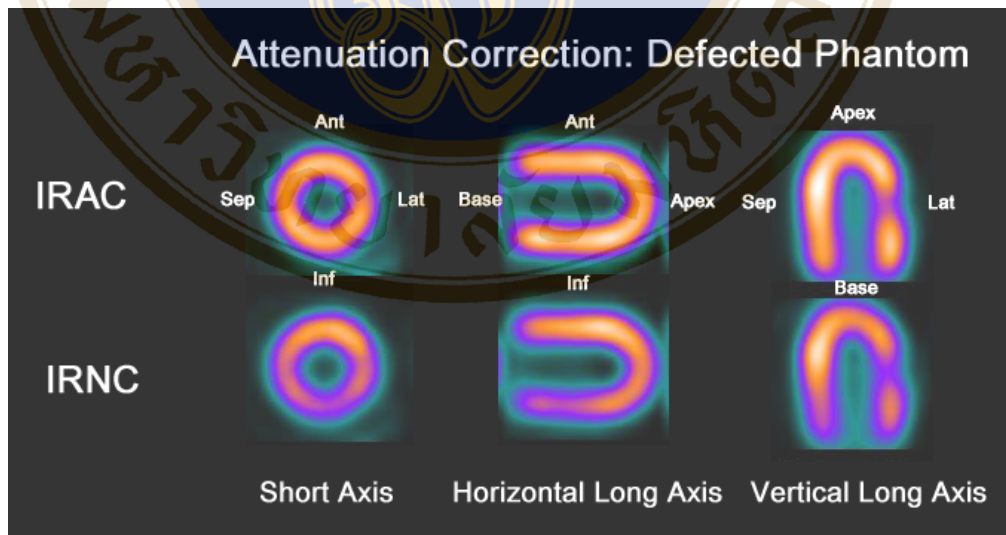


**Figure 30.** IRAC and IRNC myocardial SPECT images of solid defect phantom in lateral region of myocardial.

From Table 5 and Figure 29 IRAC images showed obvious improvements of the lesion contrast within anterior and inferior walls, but less improvement of the septal and lateral walls. However, the IRAC technique provided images with better contrast.

**5.4 Comparison of count distribution between using IRNC and IRAC technique from polar map image of cardiac phantom without solid defect.**

The comparison of polar map obtaining via IRNC and IRAC technique in normalization of count per pixel from 20 defect-free phantoms were shown in Figure 31 and Table 6, and percentage normalization versus segment were plotted as shown in Figure 32.

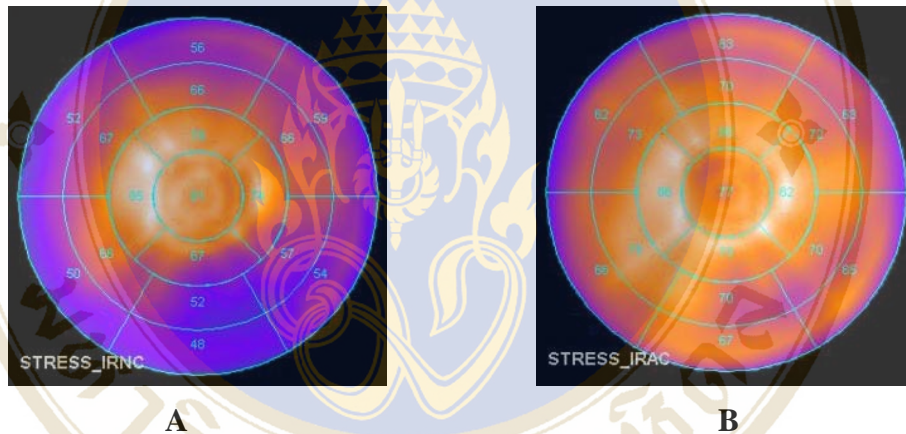


**Figure 31.** The polar map of phantom using IRNC technique (A) and IRAC technique (B)

**Table 6.** Percentage normalization from polar map with IRNC and IRAC in phantom studies.

Segment	%normalization value		p-value
	IRNC	IRAC	
1. Basal anterior	55.20±1.44	64.40±1.60	<0.001
2. Basal anteroseptal	50.65±1.18	63.55±1.64	<0.001
3. Basal inferoseptal	49.55±1.28	67.90±2.00	<0.001
4. Basal inferior	45.60±1.43	66.45±1.99	<0.001
5. Basal inferolateral	52.10±1.59	64.95±1.93	<0.001
6. Basal anterolateral	56.30±1.59	62.45±1.93	<0.001
7. Mid anterior	65.10±1.89	72.05±1.96	<0.001
8. Mid anteroseptal	67.25±1.48	76.45±2.26	<0.001
9. Mid inferoseptal	66.40±1.43	82.70±2.18	<0.001
10. Mid inferior	49.55±1.50	69.90±2.06	<0.001
11. Mid inferolateral	54.70±1.89	68.80±1.94	<0.001
12. Mid anterolateral	63.55±1.99	70.90±2.05	<0.001
13. Apical anterior	77.45±2.42	81.00±2.15	<0.001
14. Apical septal	83.00±2.10	88.60±2.30	<0.001
15. Apical inferior	64.70±1.84	80.40±2.01	<0.001
16. Apical lateral	69.90±2.10	80.75±1.94	<0.001
17. Apex	79.40±2.58	79.30±2.03	0.821

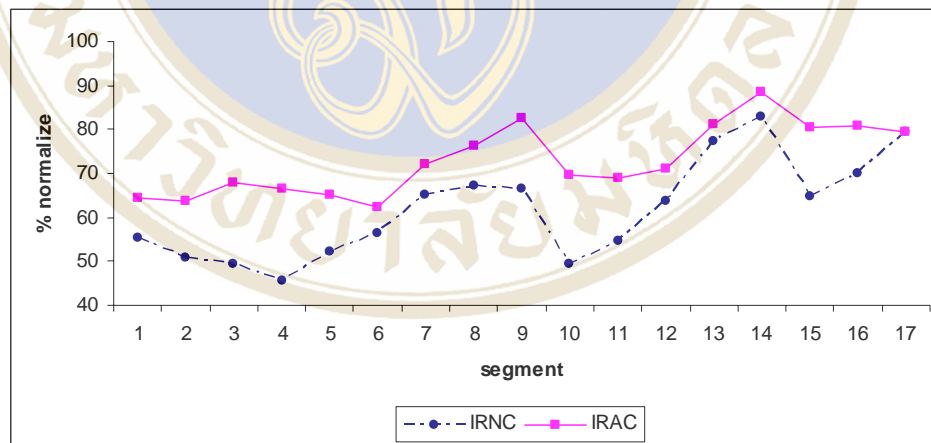


**Figure 32.** The percentage of normalization curve of IRNC and IRAC images in phantom studies.

The demonstrations of defect-free phantom SPECT images were shown in Figure 33. IRAC images improved the activity within anterior, septal, lateral, and inferior walls in comparison with IRNC images.

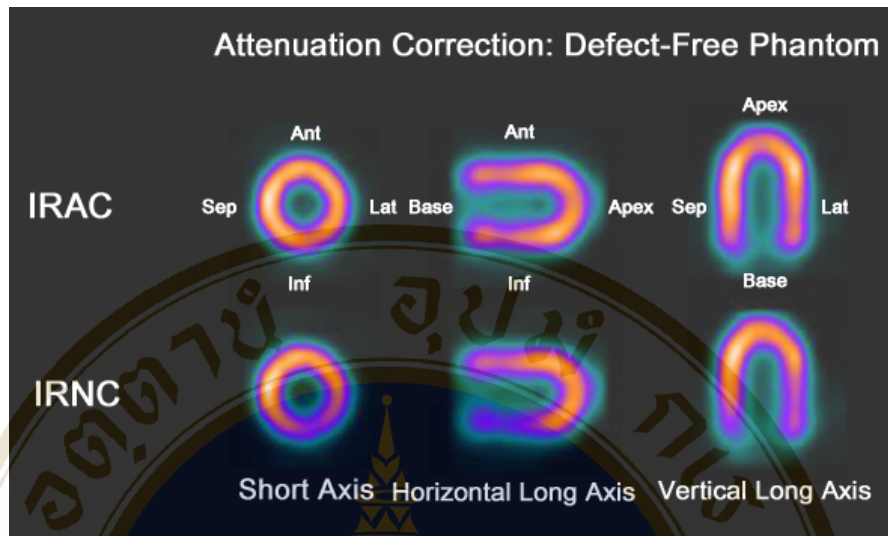


**Figure 33.** IRAC and IRNC myocardial SPECT images of defect-free phantom in lateral region of myocardial.

Table 6 showed the improvement of the normalization count per pixel in anterior, septal, lateral, and inferior walls images. The differences were significantly shown in the IRAC and IRNC images.

**Part 2: Patients studies**

**5.5 Comparison of count distribution between using IRNC and IRAC technique from polar map image of male and female patients with normal myocardium.**

**5.5.1 Male patients studies**

The comparisons of polar map of IRNC and IRAC in normalization count per pixel from 10 male patients are shown in Figure 34 and Table 7, and percentage normalization versus segment are plotted as shown in Figure 35.

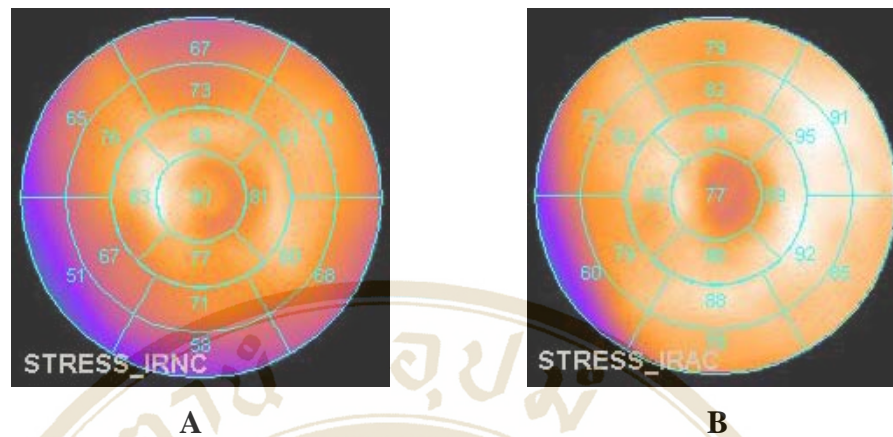


**Figure 34.** The polar map of male patient using IRNC technique (A) and IRAC technique (B).

**Table 7.** Percentage normalization from polar map with IRNC and IRAC in 10 male patients.

Segment	%normalization value		p-value
	IRNC	IRAC	
1. Basal anterior	65.70±6.61	75.00±7.68	<0.001
2. Basal anteroseptal	55.40±6.90	58.30±10.58	0.150
3. Basal inferoseptal	48.20±7.48	58.20±12.24	<0.001
4. Basal inferior	56.50±7.28	73.50±8.30	<0.001
5. Basal inferolateral	68.20±8.18	82.10±5.17	<0.001
6. Basal anterolateral	72.30±7.09	82.00±5.79	<0.001
7. Mid anterior	77.90±7.16	80.30±4.35	0.230
8. Mid anteroseptal	80.20±4.31	83.00±5.19	0.168
9. Mid inferoseptal	72.80±7.61	81.20±8.79	<0.001
10. Mid inferior	69.20±9.00	82.80±7.25	<0.001
11. Mid inferolateral	77.70±6.98	87.40±4.32	<0.001
12. Mid anterolateral	84.30±5.01	90.40±2.95	<0.001
13. Apical anterior	81.60±3.34	80.30±3.83	0.349
14. Apical septal	81.60±3.34	85.30±6.01	0.117
15. Apical inferior	77.50±8.55	81.60±6.26	0.102
16. Apical lateral	84.70±5.12	87.20±3.33	0.083
17. Apex	79.70±3.09	74.00±5.19	<0.001

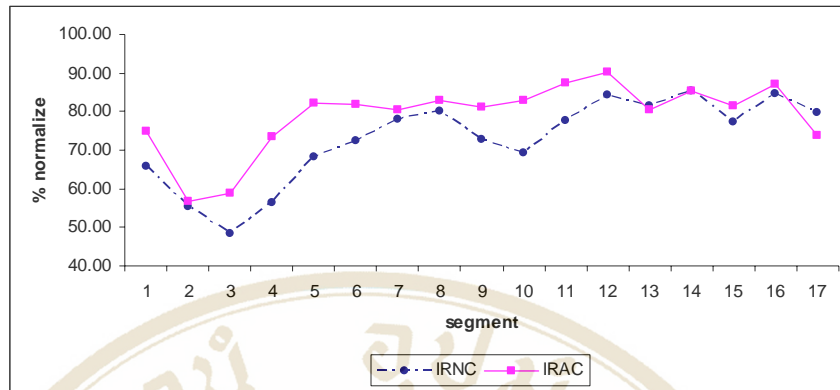


**Figure 35.** The percentage of normalization curve of IRNC and IRAC images in male patients.

The demonstrations of male SPECT images were shown in Figure 36. IRAC images improved in inferolateral, inferoseptal, lateral, and inferior walls when compared with IRNC images.

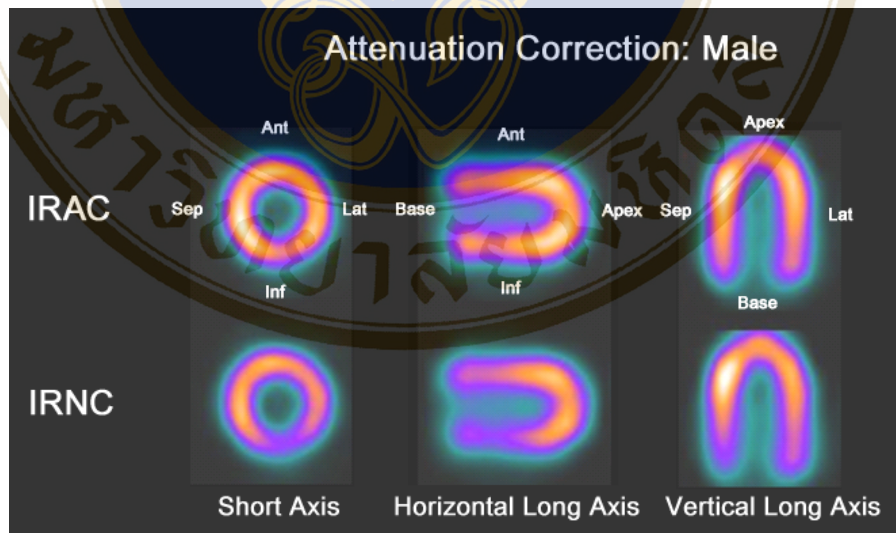


**Figure 36.** IRAC and IRNC myocardial SPECT images of male patient.

From Table 7, Figure 35, was shown that the polar map of IRAC images improved the normalization count per pixel in inferolateral, inferoseptal, lateral, and inferior walls when compared with polar map of IRNC images.

#### 5.5.1 Female patient's studies

The comparisons of polar map of IRNC and IRAC in normalization count per pixel from 10 female patients were shown in Figure 37 and Table 8, and percentage normalization versus segment were plotted as shown in Figure 38.

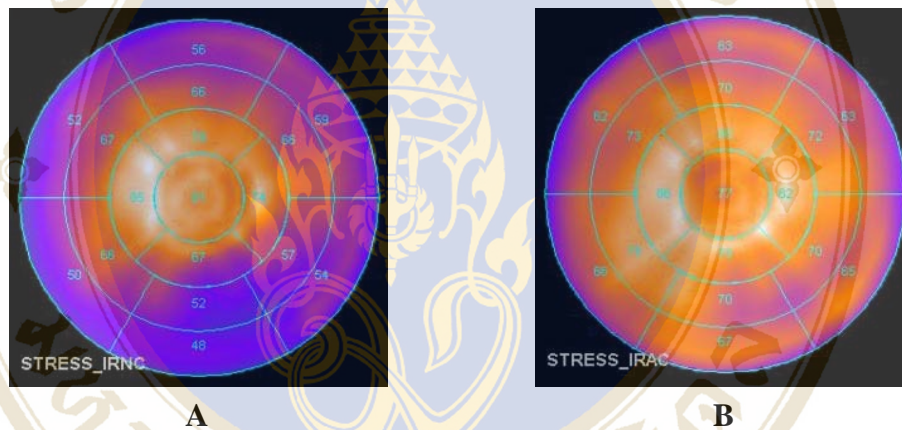


**Figure 37.** The polar map of female patient using IRNC technique (A) and IRAC technique (B).

**Table 8.** Percentage of normalization from polar map with IRNC and IRAC in 10 female patients

Segment	%normalization value		p-value
	IRNC	IRAC	
1. Basal anterior	75.40±6.93	80.10±5.97	<0.001
2. Basal anteroseptal	66.80±6.93	70.20±6.00	0.139
3. Basal inferoseptal	58.40±5.91	64.80±4.18	<0.001
4. Basal inferior	63.00±6.07	74.00±6.13	<0.001
5. Basal inferolateral	71.60±5.87	80.10±7.25	<0.001
6. Basal anterolateral	77.10±5.72	83.90±5.65	<0.001
7. Mid anterior	80.30±4.62	84.90±4.23	<0.001
8. Mid anteroseptal	86.30±5.54	88.90±3.96	0.186
9. Mid inferoseptal	79.80±5.55	85.00±3.23	<0.001
10. Mid inferior	76.00±6.09	85.50±4.72	<0.001
11. Mid inferolateral	87.70±5.20	80.80±4.83	0.064
12. Mid anterolateral	83.90±5.84	87.70±5.21	0.133
13. Apical anterior	79.00±4.57	82.50±5.33	<0.001
14. Apical septal	88.70±3.47	88.40±3.63	0.859
15. Apical inferior	81.30±4.50	84.90±3.81	<0.001
16. Apical lateral	83.80±3.52	85.00±5.25	0.460
17. Apex	81.50±5.99	76.50±6.87	<0.001

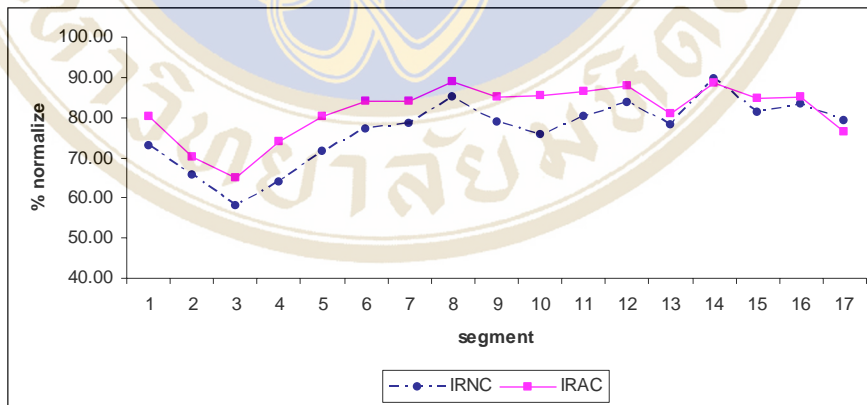


**Figure 38.** The percentage of normalization curve of IRNC and IRAC images in female patients

The demonstrations of female SPECT images were shown in Figure 39. IRAC images improved in inferolateral, inferoseptal, and anterolateral, anterior, lateral, and inferior walls when compared with IRNC images.

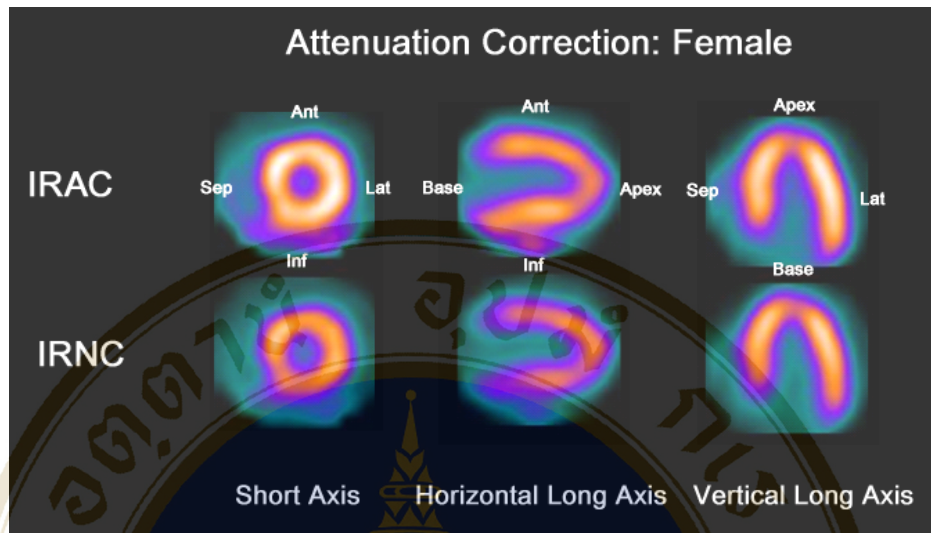


**Figure 39.** IRAC and IRNC myocardial SPECT images of female patient.

Table 8 and Figure 38 showed the resulting of female patients studies, polar map of IRAC images improved the normalization count per pixel in inferolateral, inferoseptal, anterolateral, anterior, lateral, and inferior walls when compared with polar map IRNC.

### **5.5 Comparisons of sensitivity, specificity, and accuracy between using IRNC and IRAC techniques from short axis image**

The comparisons of sensitivity, specificity and accuracy between using IRNC and IRAC techniques from short axis images that were interpreted by two observers were shown in Table 11. The ROC curve were plotted using sensitivity or true positive fraction (TPF) versus its false positive fraction (FPF=1-specificity) for all decision threshold. Table 9 and 10 showed the results of TPF and FPF from observer 1 and observer 2, respectively. Figure 40 and 41 showed the plots of ROC curve of observer 1 and observer 2, respectively.

**Table 9.** Data resulting from observer 1.

Decision Threshold	IRNC		IRAC	
	TPF	FPF	TPF	FPF
Strict	0.50	0	0.20	0
Less strict	0.55	0.15	0.40	0.05
Less lax	0.70	0.40	0.70	0.15
Lax	0.80	0.75	0.80	0.40

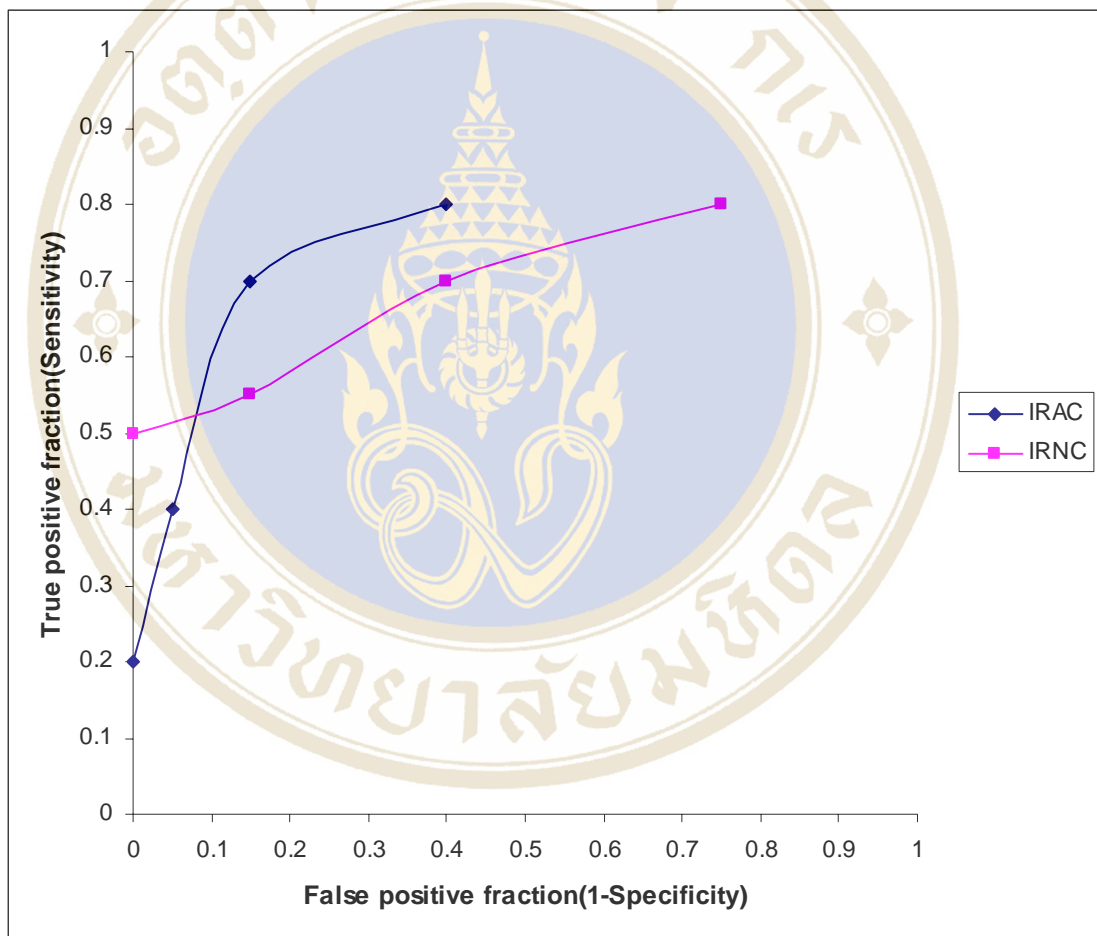


**Figure 40.** A plot of ROC curve from the observer 1's data.

**Table 10.** Data resulting from observer 2.

Decision Threshold	IRNC		IRAC	
	TPF	FPF	TPF	FPF
Strict	0	0	0.25	0
Less strict	0.6	0.15	0.5	0.05
Less lax	0.65	0.4	0.75	0.15
Lax	0.85	0.75	0.8	0.4

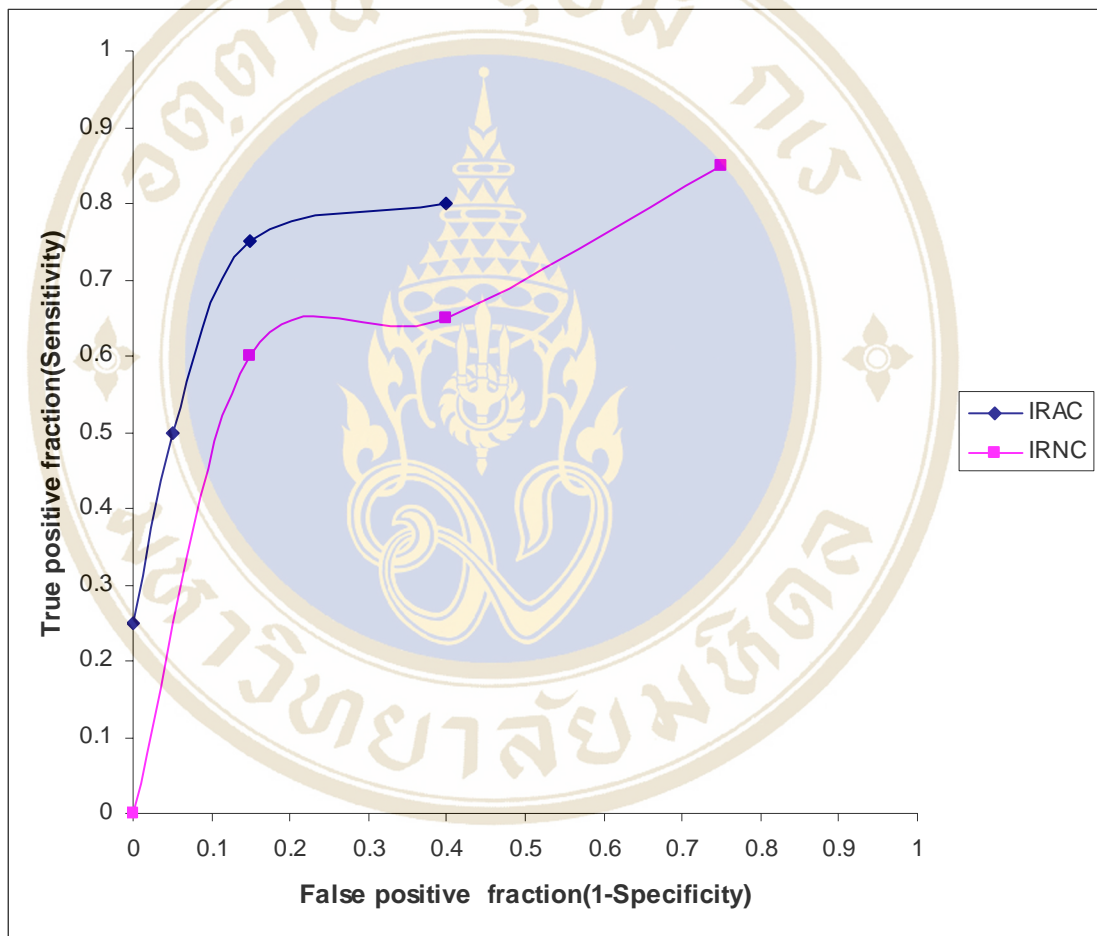


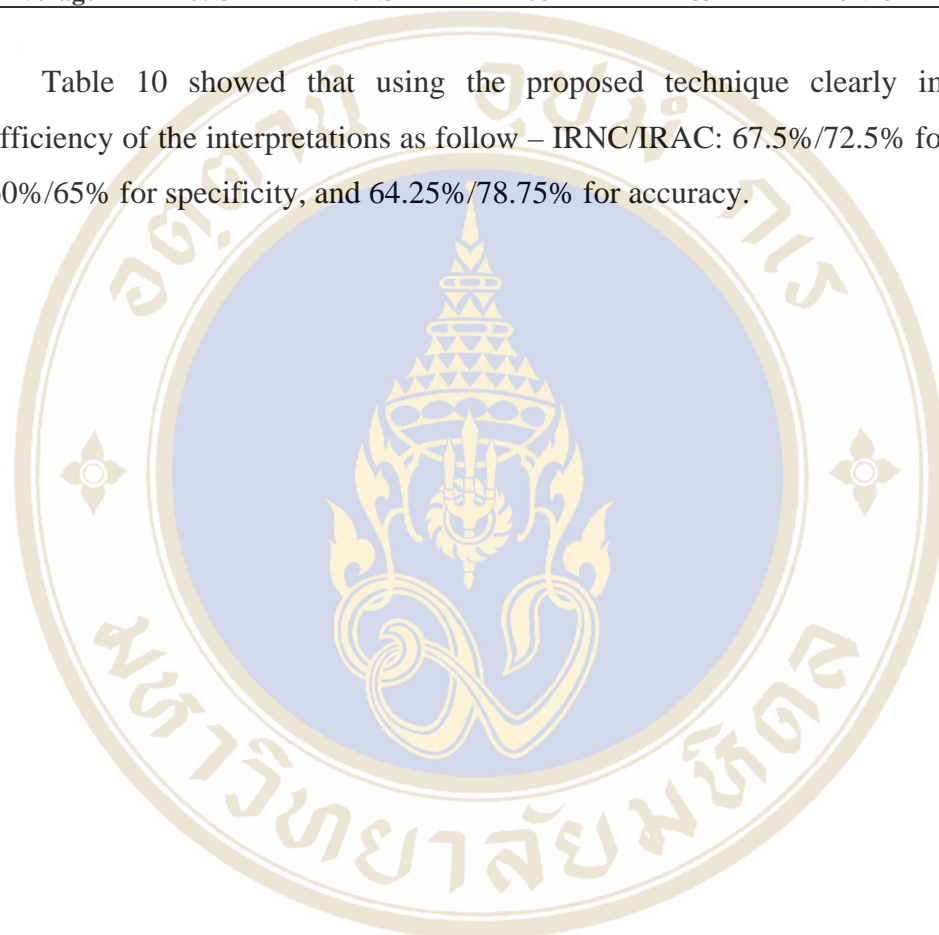
**Figure 41.** A plot of ROC curve from the observer 2’s data

From Figure 40 and 41, IRAC technique gave a better ROC curve than IRNC technique.

**Table 11.** Sensitivity, specificity, and accuracy for two observers interpreting the myocardial perfusion image using IRNC and IRAC techniques.

Observer	Sensitivity (%)		Specificity (%)		Accuracy (%)	
	IRNC	IRAC	IRNC	IRAC	IRNC	IRAC
1	70	70	60	85	65	77.5
2	65	75	60	85	62.5	80
<b>Average</b>	67.5	72.5	60	85	64.25	78.75

Table 10 showed that using the proposed technique clearly improved the efficiency of the interpretations as follow – IRNC/IRAC: 67.5%/72.5% for sensitivity, 60%/65% for specificity, and 64.25%/78.75% for accuracy.



## CHAPTER VI

### DISCUSSION

Coronary artery disease (CAD), the most important cardiac pathology which leads to chronic heart failure (CHF). Myocardial perfusion SPECT imaging, a nuclear cardiology study, has proved clinically useful in patients with know or suspected CAD. The study allows a comprehensive characterization of the extent of CAD. The artifactual heterogeneous radionuclide distributions in the patients without evidence of CAD were due to inhomogeneous attenuation of photon. The most frequently noted effects of attenuation in myocardial SPECT are artifacts associated with breast attenuation in women and diaphragmatic attenuation in men (8, 9, and 10). Attenuation correction might after the diagnostic accuracy of SPECT. This study performed iterative reconstruction non-attenuation correction (IRNC) in comparison with iterative reconstruction attenuation correction (IRAC).

Resulting myocardial phantom study depicted corrected defect size at 50% threshold level and  $2 \times 10$  numbers of update as revealed. IRAC data within Table 2, and Tale 3, respectively. The improvement of the lesion contrast within IRAC images were obviously shown in Table 4 and in Figure 27 and 29, although the lateral and septal walls produced better contrast less than 3% and 5%, respectively. The count distribution performed by IRAC technique increased significantly in Table 5.

From Table 5-7 and Figure 32, 33, 35, 36, 38, and 39, the count distribution performed by IRAC technique increased significantly especially in female anterior wall and male inferior wall which resulting from decreasing anatomical attenuation artifacts. Our results were concordant with these of Luis et al (29) and Yasmin et al (28).

The ROC curve within Table 9 and the sensitivity, specificity, and accuracy depicted in Table 10 were clearly shown the higher values obtained with IRAC technique. The results agreed well with those studied by Yasmin et al (28) and Edward et al (7).

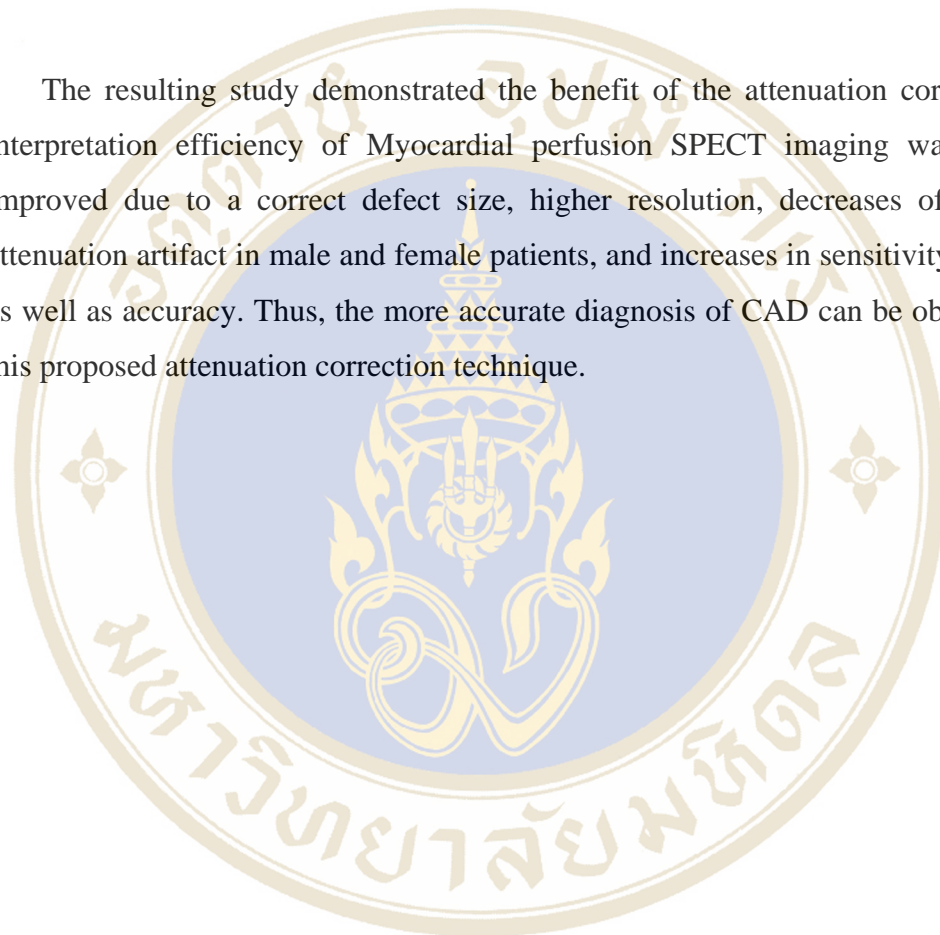
In summary, the proposed IRAC technique provided a higher diagnostic performance for the detection of CAD via SPECT imaging.



## CHAPTER VII

### CONCLUSIONS

The resulting study demonstrated the benefit of the attenuation correction. The interpretation efficiency of Myocardial perfusion SPECT imaging was obviously improved due to a correct defect size, higher resolution, decreases of anatomical attenuation artifact in male and female patients, and increases in sensitivity, specificity as well as accuracy. Thus, the more accurate diagnosis of CAD can be obtained using this proposed attenuation correction technique.



## REFERENCES

1. DePuey EG, Berman DS, Garcia EV. Cardiac SPECT imaging. New York: Raven Press, 1955:14.
2. Bouwens L, Van de Walle R, Nuyts J, Koole M, Asseler YD. Image-correction techniques in SPECT. *Comp Med Imag Grap* 2001;25: 117-26.
3. Ljungberg M, Strand S. Scatter and attenuation correction inspect using density maps and Monte Carlo simulated scatter functions. *J Nucl Med* 1990; 31(9):1560-7.
4. DePuey EG, Garcia EV. Optimal specificity of thallium-201 SPECT though recognition of imaging artifacts. *J Nucl Med* 1989; 30: 441-9.
5. Jaszczak RJ, Greer KL, Floyd CE, Harris CC, Coleman RE. Improved SPECT quantitation using compensation for scattered photons. *J Nucl Med* 1984; 25: 893-900.
6. Jaszczak RJ, Coleman RE, Whitehead FR. Physical factors an affecting quantitative measurements using camera-base single-photon emission computed tomography (SPECT). *Trans Nucl Sci* 1981; 28:69-80.
7. Ficaro EP, Fessler JA, Shreve PD, Kritzman JN, Rose PA, Corberlt JR. Simultaneous transmission/emission myocardial perfusion tomography. Diagnostic accuracy of attenuation-corrected  $^{99m}\text{Tc}$ -sestamibi single-photon emission computed tomography. *Circulation* 1996;93:463-73.
8. Sorensen SA, Phelps ME. *Physics in nuclear medicine*, ed 3, Philadelphia, WB Saunder; 1987.
9. King MA, Schwinger RB, Doherty RW, Penny BC. Two-dimensional filtering of SPECT images using the Metz and Wiener filters. *J Nucl Med* 1984; 25:1234-40.
10. Eisner RL, Nowak DJ, Pettigrew RI, Fajman W. Fundamentals of  $180^\circ$  Acquisition and reconstruction in SPECT imaging. *J Nucl Med* 1986; 27:1771-28

11. Knesaurek K, King MA, Glik SJ, Penney BC. Investigation of causes of geometric distortion in 180<sup>0</sup> and 360<sup>0</sup> angular sampling in SPECT. *J Nucl Med* 1989; 30: 1666-75.
12. Brook RA, Dichiro G. Principles of computer assisted tomography (CAT) in radiographic and radioisotopic imaging. *Phys Med Biol* 1976; 21: 689-732
13. Wilson DW, Schwinger RB, Barrett HH. Noise properties of the EM algorithm: II Monte Carlo simulations. *Phys Med Biol* 1994; 39: 847-71.
14. Jang S, Jaszczak RJ, Tsui BMW. ROC evaluation of SPECT myocardial defect detectability with and without single iteration non-uniform Chang attenuation compensation using an anthropomorphic female phantom. *IEEE Trans Nucl Sci* 1998;45:2080-8.
15. LaCroix KJ, Tsui BMW, Frey EC, Jaszczak RJ. Receiver operating characteristic evaluation of iterative reconstruction with attenuation correction in <sup>99m</sup>Tc-sestamibi myocardial SPECT Images. *J Nucl Med* 2000; 41:502-13.
16. Wells RG, King MA, Simkin PH, et al. Comparing filtered backprojection and order-subsets expectation maximization for small-lesion detection and localization in <sup>67</sup>Ga SPECT images. *J Nucl Med* 2000; 41:1391-9.
17. Wells RG, Simkin PH, Judy PF, King MA. Maximizing the detection and localization of Ga-67 tumours in thoracic SPECT MLEM (OSEM) reconstruction. *IEEE Trans Nucl Sci* 1999; 46:1191-8.
18. Wackers FJ, Berman DS, Maddahi J, et al. Technetium-99m Heaxakis 2-Methoxyisobutyl Isonitrile: Human Biodistribution, Dosimetry, Safety, and Preliminary Comparison to Thallium-201 for Myocardial Perfusion Imaging. *J Nucl Med* 1989; 30:301-11.
19. Vera P, Manrique A, Pontivianne V, et al. Thallium-Gated SPECT in Patients with Major Myocardial Infarction: Effect of Filtering and Zooming in Comparison with Equilibrium Radionuclide Imaging and Left Ventriculography. *J Nucl Med* 1999; 40: 513-21.
20. Heller GV, Links J, Bateman TM, Ziffer JA, Ficaro E, et al. American Society of Nuclear Medicine joint position statement: attenuation correction of myocardial perfusion SPECT. *J Nucl Cardiology* 2004; 11:229-30.

21. Manglos SH, Thomas FD, Gangne GM, Hellwing BJ. Phantom study of breast tissue attenuation in myocardial imaging. *J Nucl Med* 1993;34:992-6.
22. Galt JR, Cullom SJ, Garcia EV. SPECT quantification a simplified method for attenuation correction for cardiac imaging. *J Nucl Med* 1992; 33:2232-7.
23. LaCroix KJ, Tsui BMW, Frey EC, Jaszczak RJ. Receiver operating characteristic evaluation of iterative reconstruction with attenuation correction in  $^{99m}\text{Tc}$ -sestamibi myocardial SPECT images. *J Nucl Med* 2000; 41: 502-513.
24. James H. Thrall, Harvey A. Ziessman. *Nuclear Medicine, The requisites*, 2 nd ed. Mosby-Year book, Inc USA.2001; p 65-109.
25. Li Q-S, Franks TL, Franceschi D, et al. Technetium-99m methoxyisobutyl isonitrile (RP30) for quantification of myocardial ischemia and reperfusion in dogs. *J Nucl Med* 1988; 29:1939.
26. Sinusas AJ, Bergin JD, Edwards NC. Redistribution of  $^{99m}\text{Tc}$ -sestamibi and  $^{201}\text{Tl}$  in the presence of coronary artery stenosis. *Circulation*. 1994;89:2332.
27. Daisuke U, Seiji T, Shinya S, et al. Initial experience with X-ray CT base attenuation correction in myocardial perfusion SPECT imaging using a combined SPECT/CT system. *Annals of Nuclear Medicine* 2005; 19(6): 485-89.
28. Yasmin M, Yi-Hwa L, Gordon DP, et al. Clinical validation of SPECT attenuation correction using x-ray computed tomography derived attenuation maps: Multicenter clinical trial with angiographic correction. *J Nucl Car* 2005; 12(6): 676-86.
29. Luis IA, Jose M, Jimenez H, et al. Improve uniformity in tomographic myocardial perfusion imaging with attenuation correction and enhanced acquisition and processing. *J Nucl Med* 2000; 41: 1139-44.
30. Tepmongkol S, Passawang P, Krissanachinda A, Srimahachota S. The difference among stress and rest normal reference database using non-corrected, scatter corrected, and scatter with attenuation corrected bull's eye myocardial perfusion scintigraphy in both genders. *J Med Assoc Thai* 2005;88:235-41.
31. Gilland DR, Jaszczak RJ, Hanson MW, Greer KL, Coleman RE. An experimental phantom base on quantitative SPECT analysis of patient MIBI biodistribution [abstract]. *J Nucl Med* 1996; 37(suppl): 154P.

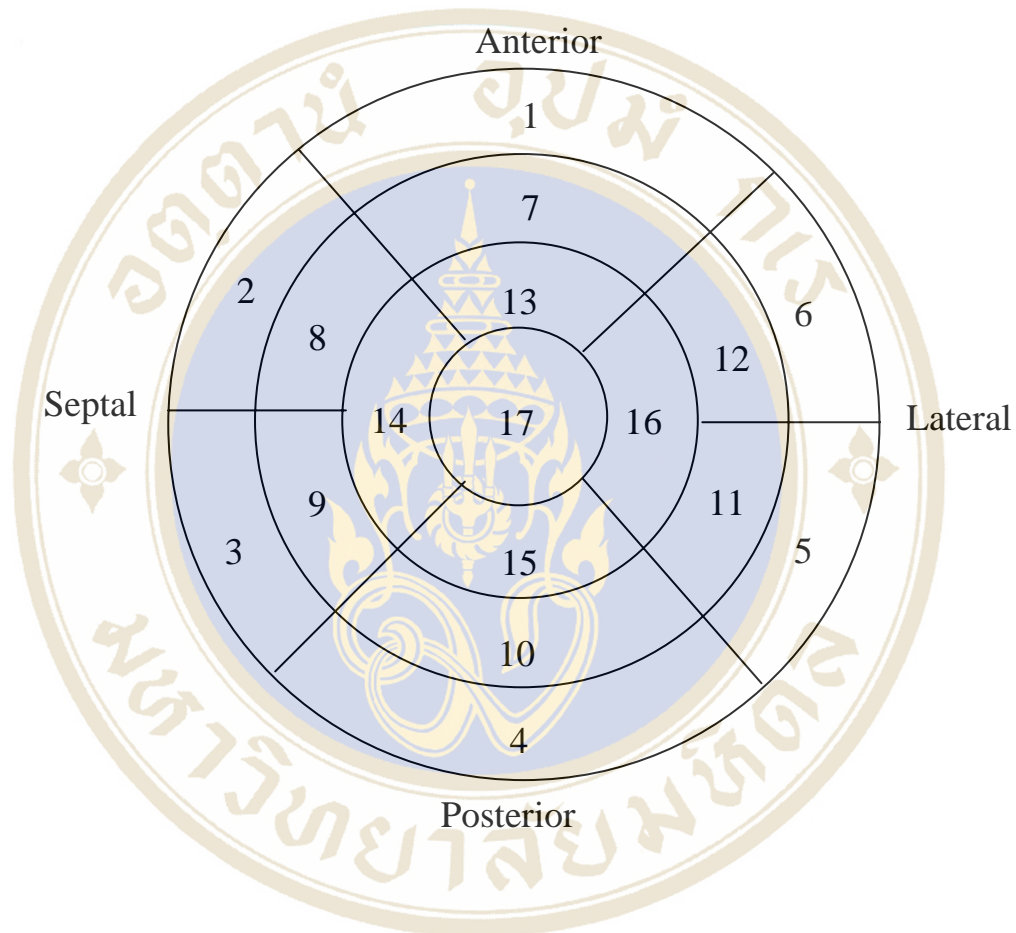
32. Germano G. Technical aspects of myocardial SPECT imaging. J Nucl Med 2001; 42: 1449-1507.





## APPENDIX A

### Diagram of polar map (17 segments)



- |                        |                       |
|------------------------|-----------------------|
| 1. basal anterior      | 10. mid inferior      |
| 2. basal anteroseptal  | 11. mid inferolateral |
| 3. basal inferoseptal  | 12. mid anterolateral |
| 4. basal inferior      | 13. apical anterior   |
| 5. basal inferolateral | 14. apical septal     |
| 6. basal anterolateral | 15. apical inferior   |
| 7. mid anterior        | 16. apical lateral    |
| 8. mid anteroseptal    | 17. apex              |
| 9. mid inferoseptal    |                       |

**APPENDIX B****Maximum Count, Minimum Count and Average Counts/Pixel in the Myocardial Area of  $^{99m}\text{Tc}$ -MIBI SPECT images.****IRNC Techniques**

Myocardial Wall	Max. Counts/Pixel	Min. Counts/Pixel	Average Counts/Pixel
Anterior	800	85	491.48
Inferior	708	190	446.64
Lateral	800	84	358.45
Septal	837	167	551.39

**IRAC Techniques**

Myocardial Wall	Max. Counts/Pixel	Min. Counts/Pixel	Average Counts/Pixel
Anterior	2476	424	1503.57
Inferior	2518	352	1538.41
Lateral	2348	206	1053.91
Septal	2801	637	1655.30

## APPENDIX C

### Counts per Pixel in 17 Segments of Cardiac Phantom with solid defect applying IRNC and IRAC technique

#### IRNC Technique

Phantom	Segment																
	1	2	3	4	5	6	7	8	9	10	11	12	13	14	15	16	17
1	56	52	50	48	54	59	66	67	66	52	57	66	79	85	67	74	81
2	56	51	50	45	53	57	66	68	67	50	55	64	79	84	65	70	81
3	56	50	49	47	53	57	66	68	67	50	56	65	78	84	66	71	81
4	56	51	50	45	53	57	66	68	67	50	55	64	79	84	65	70	81
5	55	49	47	44	51	55	64	65	64	47	55	63	76	80	63	69	78
6	56	50	49	47	53	57	66	68	67	50	56	65	78	84	66	71	81
7	54	51	50	46	51	56	64	67	66	49	53	62	76	82	64	69	78
8	56	52	50	47	53	57	66	67	67	50	56	65	78	84	65	72	79
9	54	49	48	45	51	55	64	66	65	48	54	63	75	81	64	68	78
10	55	50	48	44	51	55	65	65	65	47	55	62	76	81	63	69	77
11	53	49	48	44	50	54	62	66	65	49	52	61	74	80	62	67	75
12	54	50	49	43	50	54	63	65	65	48	52	60	75	81	62	67	76
13	54	50	50	44	51	55	64	67	66	49	53	62	77	82	63	68	78
14	58	51	50	47	55	59	69	70	69	51	58	67	83	87	68	73	85
15	54	51	50	46	51	56	64	67	66	49	53	62	76	82	64	69	78
16	54	51	50	46	51	56	64	68	66	49	53	63	76	82	64	69	80
17	56	54	53	48	53	57	66	69	69	53	56	65	79	85	67	72	80
18	58	51	51	46	55	59	69	70	69	51	58	67	82	87	68	73	84
19	53	50	49	45	50	54	62	66	65	49	52	61	74	81	63	67	76
20	56	51	50	45	53	57	66	68	67	50	55	64	79	84	65	70	81

**IRAC Technique**

Phantom	Segment																
	1	2	3	4	5	6	7	8	9	10	11	12	13	14	15	16	17
1	63	62	66	67	65	63	70	73	79	70	70	72	80	86	79	82	77
2	66	65	70	67	68	65	75	78	85	71	71	73	84	91	82	83	81
3	67	65	69	68	67	65	74	79	85	71	71	74	82	91	83	83	81
4	66	65	70	67	68	65	75	78	85	71	71	73	84	91	82	83	81
5	62	59	62	62	62	59	69	71	78	64	67	68	77	83	76	77	75
6	67	65	69	68	67	65	74	79	85	71	71	74	82	91	83	83	81
7	64	64	69	67	65	62	72	77	83	70	68	71	81	89	81	81	80
8	63	62	66	65	63	61	70	74	80	67	68	70	79	86	79	80	77
9	66	65	70	68	67	65	74	79	85	70	71	74	82	90	83	83	81
10	63	62	65	63	62	60	71	73	80	66	67	69	80	86	78	79	78
11	64	65	69	67	64	62	71	77	83	69	67	70	79	88	80	79	78
12	63	63	67	63	62	60	70	75	81	68	65	68	80	87	78	78	78
13	63	63	68	65	64	61	72	76	82	69	67	69	81	88	79	79	79
14	66	63	68	66	66	64	74	78	84	71	71	72	84	91	82	82	82
15	64	64	68	68	65	62	71	77	83	70	68	70	80	89	80	80	79
16	64	64	68	68	64	62	71	77	83	70	68	69	80	89	80	80	79
17	64	66	70	70	65	62	72	77	84	73	70	71	81	89	82	82	80
18	66	62	68	66	66	63	74	78	84	71	70	72	84	91	82	82	82
19	62	63	67	67	63	60	69	75	81	69	66	68	77	86	78	78	76
20	65	64	69	67	66	63	73	78	84	71	69	71	83	90	81	81	81

## APPENDIX D

**Counts per Pixel in 17 Segments of 10 Normal Male Patients  
applying IRNC and IRAC technique**

**IRNC Technique**

Patients	Segment																
	1	2	3	4	5	6	7	8	9	10	11	12	13	14	15	16	17
1	67	65	51	58	68	74	73	76	67	71	80	81	83	83	77	81	80
2	61	49	39	52	68	70	82	81	65	63	77	86	86	83	74	89	84
3	60	70	64	54	61	64	77	90	85	72	73	83	87	90	79	88	78
4	66	52	52	61	65	69	74	75	73	71	76	81	83	88	78	83	82
5	73	54	54	57	74	80	75	79	76	60	72	81	81	88	86	77	81
6	63	54	44	53	74	75	75	80	63	65	82	85	78	77	66	81	77
7	58	48	39	43	52	61	74	81	68	60	66	80	80	85	66	79	74
8	75	55	46	67	78	81	90	82	81	84	88	93	81	88	89	91	82
9	75	55	46	67	78	81	90	82	81	84	88	93	81	88	89	91	82
10	59	52	47	53	64	68	69	76	69	62	75	80	76	83	71	87	77

**IRAC Technique**

Patients	Segment																
	1	2	3	4	5	6	7	8	9	10	11	12	13	14	15	16	17
1	80	73	60	78	85	91	82	83	79	88	92	95	84	85	86	89	77
2	78	44	44	69	80	76	79	76	68	78	85	92	84	81	77	89	76
3	74	70	81	80	88	82	75	88	92	90	88	89	79	85	84	88	70
4	75	55	68	90	83	83	81	80	88	93	90	91	81	91	89	88	76
5	78	55	69	72	89	91	80	88	90	73	85	90	83	94	75	84	77
6	70	46	46	61	81	75	73	75	65	76	90	86	72	72	73	82	67
7	70	55	55	66	72	77	79	86	81	77	79	90	78	86	74	83	68
8	76	55	52	78	86	86	88	79	82	91	94	94	77	83	89	89	69
9	74	56	53	68	79	79	85	89	84	84	85	86	83	87	86	87	83
10	75	60	60	73	78	80	81	86	83	78	86	91	82	89	83	93	77

### APPENDIX E

#### Counts per Pixel in 17 Segments of 10 Normal Female Patients applying IRNC and IRAC technique

##### IRNC Technique

Patients	Segment																
	1	2	3	4	5	6	7	8	9	10	11	12	13	14	15	16	17
1	71	67	50	55	66	70	75	84	71	70	81	80	81	87	76	86	83
2	82	64	61	66	71	80	84	91	85	84	90	89	76	91	86	85	83
3	82	63	58	63	73	85	87	78	76	74	90	95	81	81	78	88	81
4	76	72	59	60	78	73	81	93	84	74	85	78	80	92	84	83	89
5	79	73	66	66	71	77	86	92	87	80	90	79	81	88	82	80	83
6	71	63	56	65	72	77	72	78	78	77	90	79	67	87	76	77	67
7	82	80	64	63	64	83	80	90	82	77	86	84	82	90	84	82	79
8	81	69	66	76	84	84	80	89	85	84	87	91	82	92	89	88	87
9	66	56	51	55	70	71	79	85	77	64	88	81	79	92	77	83	84
10	64	61	53	61	67	71	79	83	73	76	90	83	81	87	81	86	79

##### IRAC Technique

Patients	Segment																
	1	2	3	4	5	6	7	8	9	10	11	12	13	14	15	16	17
1	85	76	58	69	81	84	88	94	83	87	95	93	88	92	92	88	77
2	82	70	73	79	81	86	84	87	88	93	86	87	83	82	82	88	80
3	82	64	61	66	71	80	88	91	85	84	83	89	83	91	91	86	70
4	77	69	65	72	88	79	81	90	87	81	89	80	86	90	90	85	75
5	76	67	68	77	82	80	86	91	92	90	86	82	85	87	87	84	79
6	81	72	68	80	85	90	77	80	82	85	86	89	69	82	82	76	79
7	91	74	62	80	80	95	88	90	84	87	86	95	85	90	90	89	75
8	82	80	64	63	64	83	80	90	82	77	75	84	82	90	90	84	70
9	69	59	64	77	85	76	81	85	85	82	86	84	79	91	91	82	85
10	76	71	65	77	84	86	89	91	82	89	94	94	85	89	89	87	75

## APPENDIX F

### Sensitivity, Specificity and Accuracy of Interpretation Reported by Observer 1 and Observer 2

#### Confidence Rating Scale

Rating Scale	Confidence
0	Normal
1	Slight reduction of Tc-99m sestamibi uptake
2	Moderate reduction of uptake, usually implying significant abnormality
3	Severe reduction of uptake
4	Absence Tc-99m sestamibi uptake

#### Decision Threshold

Decision Threshold	Categories considered	
	Positive or Abnormal or T+	Negative or Normal or T-
1. Strict	Definitely. Abnormal 4	0,1,2,3
2. Less Strict	3,4	0,1,2
3. Less Lax	2,3,4	0,1
4. Lax	1,2,3,4	Definitely. Normal 0

Diagnostic test result	Gold standard	
	Present (D+)	Absent (D-)
Abnormal test (T+)	True Positive (TP)	False Positive (FP)
Normal (T-)	False Negative (FN)	True Negative (TN)

**Observer 1**

**The result of interpretation for patient based myocardial perfusion.**

No.	Abnormal patient		No.	Normal patient	
	IRNC	IRAC		IRNC	IRAC
1	4	4	1	3	2
2	4	3	2	0	1
3	4	2	3	1	0
4	4	4	4	2	1
5	4	3	5	1	0
6	4	4	6	1	0
7	2	2	7	1	1
8	4	3	8	1	1
9	0	0	9	2	0
10	4	3	10	2	3
11	3	2	11	2	0
12	4	4	12	1	1
13	4	2	13	0	0
14	2	2	14	3	2
15	0	0	15	0	0
16	1	0	16	0	0
17	0	1	17	1	0
18	2	1	18	2	0
19	1	0	19	0	0
20	0	2	20	3	0

**The result of interpretation for coronary angiography.**

No.	Abnormal patient		No.	Normal patient	
	Positive	Negative		Positive	Negative
1	Yes	No	1	No	Yes
2	Yes	No	2	No	Yes
3	Yes	No	3	No	Yes
4	Yes	No	4	No	Yes
5	Yes	No	5	No	Yes
6	Yes	No	6	No	Yes
7	Yes	No	7	No	Yes
8	Yes	No	8	No	Yes
9	Yes	No	9	No	Yes
10	Yes	No	10	No	Yes
11	Yes	No	11	No	Yes
12	Yes	No	12	No	Yes
13	No	Yes	13	No	Yes
14	No	Yes	14	No	Yes
15	Yes	No	15	No	Yes
16	Yes	No	16	No	Yes
17	Yes	No	17	No	Yes
18	No	Yes	18	No	Yes
19	No	Yes	19	No	Yes
20	Yes	No	20	No	Yes

**The result of rating of confidence.**

Confidence	IRNC		IRAC	
	T+	T-	T+	T-
0	4	5	4	12
1	2	7	2	5
2	3	5	6	2
3	1	3	4	1
4	10	0	4	0

**The result of decision threshold.**

▪ **IRNC**

Strict			Less Strict			Less Lax			Lax		
	D+	D-		D+	D-		D+	D-		D+	D-
T+	10	0	T+	11	3	T+	14	8	T+	16	15
T-	10	20	T-	9	17	T-	6	12	T-	4	5

▪ **IRAC**

Strict			Less Strict			Less Lax			Lax		
	D+	D-		D+	D-		D+	D-		D+	D-
T+	4	0	T+	8	1	T+	14	3	T+	16	8
T-	16	20	T-	12	19	T-	6	17	T-	4	12

**The result of decision threshold.**

▪ **IRNC**

Decision Threshold	Raw Data				Decision Threshold	Calculated Data			
	IRNC					IRNC			
	TPF	FPF	TNF	FNF		TPF	FPF	TNF	FNF
Strict	10/20	0/20	10/20	20/20	Strict	0.5	0	0.5	1
Less strict	11/20	3/20	9/20	17/20	Less strict	0.55	0.15	0.45	0.85
Less lax	14/20	8/20	6/20	12/20	Less lax	0.7	0.4	0.3	0.6
Lax	16/20	15/20	4/20	5/20	Lax	0.8	0.75	0.2	0.25

▪ **IRAC**

Decision Threshold	Raw Data				Decision Threshold	Calculated Data			
	IRAC					IRAC			
	TPF	FPF	TNF	FNF		TPF	FPF	TNF	FNF
Strict	4/20	0/20	16/20	20/20	Strict	0.2	0	0.8	1
Less strict	8/20	1/20	12/20	19/20	Less strict	0.4	0.05	0.6	0.95
Less lax	14/20	3/20	6/20	17/20	Less lax	0.7	0.15	0.3	0.85
Lax	16/20	8/20	4/20	12/20	Lax	0.8	0.4	0.2	0.6

**The result of sensitivity, specificity and accuracy.**

Decision Threshold	Sensitivity		Specificity		Accuracy	
	IRNC	IRAC	IRNC	IRAC	IRNC	IRAC
Strict	50	20	100	100	75	60
Less strict	55	40	85	95	70	67.5
Less lax	70	70	60	85	65	77.5
Lax	80	80	25	60	52.5	70

**Observer 2**

**The result of interpretation for patient based myocardial perfusion.**

No.	Abnormal patient		No.	Normal patient	
	IRNC	IRAC		IRNC	IRAC
1	3	4	1	3	3
2	3	4	2	0	1
3	3	2	3	1	1
4	3	4	4	2	2
5	3	3	5	1	0
6	3	4	6	1	0
7	3	1	7	1	0
8	3	3	8	1	1
9	1	0	9	2	1
10	3	3	10	2	0
11	2	3	11	2	0
12	3	3	12	1	1
13	3	4	13	0	0
14	0	2	14	3	2
15	1	0	15	0	0
16	1	0	16	0	0
17	3	2	17	1	0
18	0	2	18	2	0
19	0	0	19	0	0
20	1	2	20	3	0

**The result of interpretation for coronary angiography.**

No.	Abnormal patient		No.	Normal patient	
	Positive	Negative		Positive	Negative
1	Yes	No	1	No	Yes
2	Yes	No	2	No	Yes
3	Yes	No	3	No	Yes
4	Yes	No	4	No	Yes
5	Yes	No	5	No	Yes
6	Yes	No	6	No	Yes
7	Yes	No	7	No	Yes
8	Yes	No	8	No	Yes
9	Yes	No	9	No	Yes
10	Yes	No	10	No	Yes
11	Yes	No	11	No	Yes
12	Yes	No	12	No	Yes
13	No	Yes	13	No	Yes
14	No	Yes	14	No	Yes
15	Yes	No	15	No	Yes
16	Yes	No	16	No	Yes
17	Yes	No	17	No	Yes
18	No	Yes	18	No	Yes
19	No	Yes	19	No	Yes
20	Yes	No	20	No	Yes

**The result of rating method.**

Confidence	IRNC		IRAC	
	T+	T-	T+	T-
0	3	5	4	12
1	4	7	1	5
2	1	5	5	2
3	12	3	5	1
4	0	0	5	0

**The result of decision threshold.**

▪ IRNC

Strict			Less Strict			Less Lax			Lax		
	D+	D-		D+	D-		D+	D-		D+	D-
T+	0	0	T+	12	3	T+	13	8	T+	17	15
T-	20	20	T-	8	17	T-	7	12	T-	3	5

▪ IRAC

Strict			Less Strict			Less Lax			Lax		
	D+	D-		D+	D-		D+	D-		D+	D-
T+	5	0	T+	10	1	T+	15	3	T+	16	8
T-	15	20	T-	10	19	T-	5	17	T-	4	12

**The result of decision threshold.**

▪ IRNC

Decision Threshold	Raw Data				Decision Threshold	Calculated Data			
	IRNC					IRNC			
	TPF	FPF	TNF	FNF		TPF	FPF	TNF	FNF
Strict	0/20	0/20	20/20	20/20	Strict	0	0	1	1
Less strict	12/20	3/20	8/20	17/20	Less strict	0.6	0.15	0.4	0.85
Less lax	13/20	8/20	7/20	12/20	Less lax	0.65	0.4	0.35	0.6
Lax	17/20	15/20	3/20	5/20	Lax	0.85	0.75	0.15	0.25

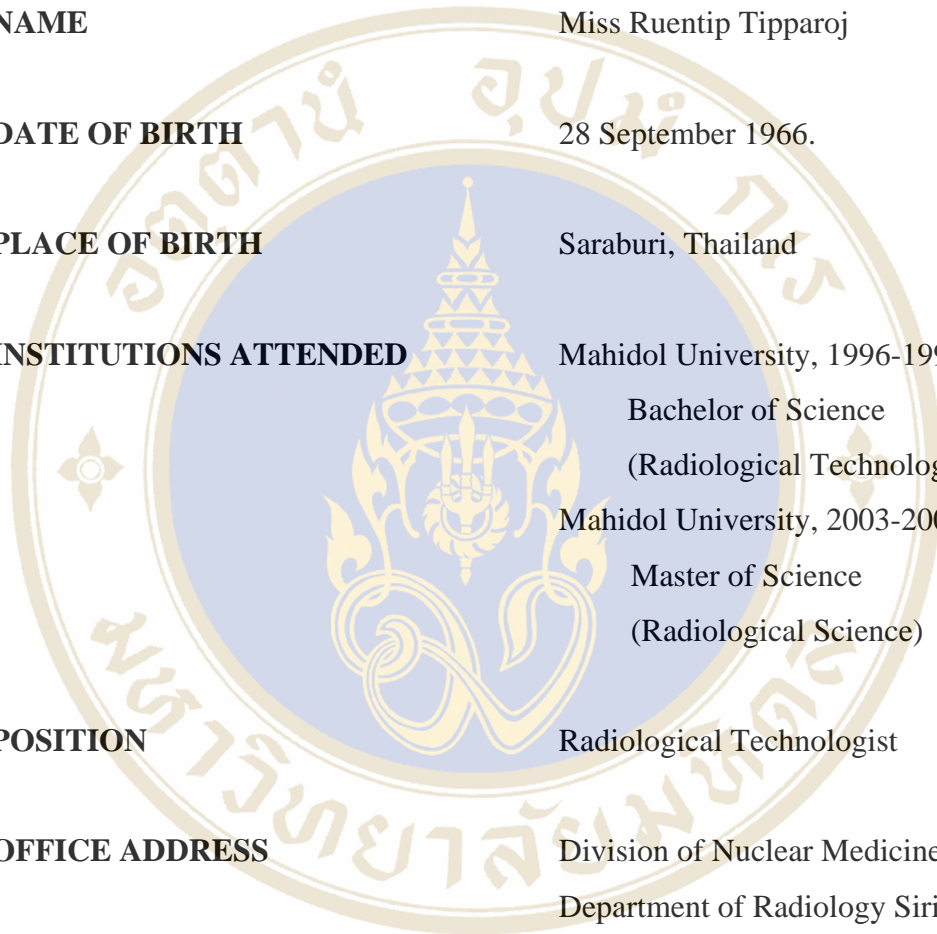
▪ IRAC

Decision Threshold	Raw Data				Decision Threshold	Calculated Data			
	IRAC					IRAC			
	TPF	FPF	TNF	FNF		TPF	FPF	TNF	FNF
Strict	5/20	0/20	15/20	20/20	Strict	0.25	0	0.75	1
Less strict	10/20	1/20	10/20	19/20	Less strict	0.5	0.05	0.5	0.95
Less lax	15/20	3/20	5/20	17/20	Less lax	0.75	0.15	0.25	0.85
Lax	16/20	8/20	4/20	12/20	Lax	0.8	0.4	0.2	0.6

**The result of sensitivity, specificity and accuracy.**

Decision Threshold	Sensitivity		Specificity		Accuracy	
	IRNC	IRAC	IRNC	IRNC	IRAC	IRNC
Strict	0	25	100	100	50	62.5
Less strict	60	50	85	95	72.5	72.5
Less lax	65	75	60	85	62.5	80
Lax	85	80	25	60	55	70

## BIOGRAPHY



<b>NAME</b>	Miss Ruentip Tipparoj
<b>DATE OF BIRTH</b>	28 September 1966.
<b>PLACE OF BIRTH</b>	Saraburi, Thailand
<b>INSTITUTIONS ATTENDED</b>	Mahidol University, 1996-1998 Bachelor of Science (Radiological Technology) Mahidol University, 2003-2008 Master of Science (Radiological Science)
<b>POSITION</b>	Radiological Technologist
<b>OFFICE ADDRESS</b>	Division of Nuclear Medicine Department of Radiology Siriraj Hospital Bangkok, Thailand 10700. Tel. 024196180-1